Comparison of novel semi-airborne electromagnetic data with multi-scale geophysical, petrophysical and geological data from Schleiz, Germany

Annika Steuer [a],[*], Maria Smirnova [b], Michael Becken [b], Markus Schiffler [c], Thomas Günther [e], Raphael Rochlitz [e], Pritam Yogeshwar [d], Wiebke Mörbe [d], Bernhard Siemon [a], Stephan Costabel [a], Benedikt Preugschat [a], Malte Ibs-von Seht [a], Luigi Sante Zampa [a,g], Franz Müller [f]

[a] Federal Institute for Geosciences and Natural Resources (BGR), Stilleweg 2, D-30655 Hannover, Germany
[b] Institute of Geophysics, University of Münster (WWU), Corrensstr. 24, D-48149 Münster, Germany
[c] Leibniz Institute of Photonic Technology (Leibniz IPHT), Albert-Einstein-Straße 9, D-07745 Jena, Germany
[d] Institute of Geophysics and Meteorology, University of Cologne (UoC), Pohligstr. 3, D-50969 Köln, Germany
[e] Leibniz Institute for Applied Geophysics (LIAG), Stilleweg 2, D-30655 Hannover, Germany
[f] Technische Bergakademie Freiberg (TUBAF), Bernhard-v.-Cotta-Str. 2, D-09599 Freiberg, Germany
[g] Istituto Nazionale di Oceanografia e di Geofisica Sperimentale (OGS), via Beirut 2, 34014 Trieste, Italy

ARTICLE INFO

ABSTRACT

In the framework of the Deep Electromagnetic Sounding for Mineral EXploration (DESMEX) project, we carried out multiple geophysical surveys from regional to local scales in a former mining area in the state of Thuringia, Germany. We prove the applicability of newly developed semi-airborne electromagnetic (EM) systems for mineral exploration by cross-validating inversion results with those of established airborne and ground-based investigation techniques. In addition, supporting petrophysical and geological information to our geophysical measurements allowed the synthesis of all datasets over multiple scales.

An initial regional-scale reconnaissance survey was performed with BGR's standard helicopter-borne geophysical system deployed with frequency-domain electromagnetic (HEM), magnetic and radiometric sensors. In addition to geological considerations, the HEM results served as base-line information for the selection of an optimal location for the intermediate-scale semi-airborne EM experiments. The semi-airborne surveys utilized long grounded transmitters and two independent airborne receiver instruments: induction coil magnetometers and SQUID sensors. Due to the limited investigation depth of the HEM method, local-scale electrical resistivity tomography (ERT) and long-offset transient electromagnetic (LOTEM) measurements were carried out on a reference profile, enabling the validation of inversion results at greater depths.

The comparison of all inversion results provided a consistent overall resistivity distribution. It further confirmed that both semi-airborne receiver instruments achieve the bandwidth and sensitivity required for the investigation of the resistivity structure down to 1 km depth and therewith the detection of deeply seated earth resources. A 3D geological model, lithological and geophysical borehole logs as well as petrophysical investigations were integrated to interpret the geophysical results. Distinct highly-conductive anomalies with resistivities of less than 10 Ωm were identified as alum shales over all scales. Apart from that, the petrophysical investigations exhibited that correlating geophysical and geological information using only one single parameter, such as the electrical resistivity, is hardly possible. Therefore, we developed a first approach based on clustering methods and self-organizing maps (SOMs) that allowed us to assign geological units at the surface to a given combination of geophysical and petrophysical parameters, obtained on different scales.

1. Introduction

The increasing demand for mineral resources in recent years requires the development of new competitive methods and technologies for geophysical exploration. Previous mining of mineral resources took place in the upper hundred meters below the surface, whereas

* Corresponding author.
  E-mail address: annika.steuer@bgr.de (A. Steuer).

today, new techniques are being actively evolved to facilitate deeper exploration (Zhdanov, 2010; Vallée et al., 2011; Smith, 2014). This should provide knowledge about the full spatial extent of prospective geological structures, including their depth extension.

Airborne electromagnetic (EM) methods are well established in mineral exploration because they are fast and relatively inexpensive (Fountain, 1998; Smith, 2014). However, pure airborne EM methods are often not suitable to achieve sufficiently large penetration depths because of the limited transmitter power, reduced coupling with the ground and motional noise. The semi-airborne EM concept combines the advantages of powerful ground-based electric dipole transmitters with high-resolution airborne magnetic field receivers (Elliott, 1996; Mogi et al., 1998; Smith et al., 2001; Yang and Oldenburg, 2016). Wu et al. (2019) presented a review on semi-airborne EM developments and applications in China. These studies show that a semi-airborne EM survey design is feasible and allows for achieving increased investigation depth in comparison to traditional airborne EM systems.

A German consortium, comprising the Federal Institute for Geosciences and Natural Resources (BGR), three universities, two research institutes and two companies, established the Deep Electromagnetic Sounding for Mineral Exploration (DESMEX) project (Becken et al., 2020). We used multiple geophysical methods to verify the results of two new semi-airborne EM receiver systems. The surveys were carried out on various scales, illustrated in Fig. 1, in a former mining area in eastern Germany. In the regional-scale, preliminary investigation (445 km^2) with the helicopter-borne geophysical system of BGR, the established methods of frequency-domain electromagnetics (HEM), magnetics (HMG) and radiometrics (HRD) were applied (Steuer et al., 2016; Martin et al., 2017). The data allowed the determination of the electrical conductivity distribution and the magnetic properties of the subsurface, and the radionuclides of the near-surface material, respectively. HEM, e.g., enables investigation down to a depth of 150 m. The regional scale also includes existing ground-based gravimetric data, which are available throughout Germany from the Leibniz Institute for Applied Geophysics (LIAG, 2010; Skiba, 2011). The semi-airborne EM method requires a transmitter on the ground and is more appropriate for an intermediate scale (in this case 74 km^2), with a much greater investigation depth (of the order of 1 km) than the HEM method. Local-scale ground-based validation studies such as electrical resistivity tomography (ERT) (Oppermann and Günther, 2018) and long-offset transient electromagnetics (LOTEM) (Mörbe et al., 2020) were carried out on 7.5 and 8.5 km long profiles, respectively, to verify the semi-airborne EM results at depth. These local-scale EM methods are able to explore the subsurface down to a depth of 1 km. However, they require transmitters and receivers placed on the ground, leading usually only to 2D information in comparatively small areas to be covered and areal investigation is not possible in a reasonable time. Borehole geophysics was also acquired on a local scale and provided petrophysical information of the different geological formations of the survey area (Pechnig, 2019). Furthermore, petrophysical laboratory tests on rock samples were performed to evaluate the geophysical results and interpret the subsurface models (Martin et al., 2016; Costabel and Martin, 2019).

We begin describing the geological and petrophysical settings in the survey area. We continue with the description of the EM methods and the surveys carried out. The presentation of the results has two focuses. Firstly, we concentrate on the multi-scale EM. We show 2D inversion results of all EM methods that were verified against each other in a single section, and a perspective 3D view of the resistivity models to illustrate the different scales. Secondly, we present an integrated interpretation method of the regional-scale geophysical results by a statistical approach. The developed method uses self-organizing maps (SOMs) to detect patterns in the distribution of resistivity, magnetic susceptibility, natural gamma radiation and gravity related to regional geological structures. Finally, we discuss the general comparability of the different EM methods and the limits of clustering. The appendix contains a lithostratigraphic table, the methodological descriptions of HMG, HRD and gravimetry, as well as data plots of all resistivity methods.

2. Geology of the survey area

We chose a former mining region within the Thuringian-Saxon slate mountains in eastern Germany for the preliminary investigation with helicopter-borne geophysics. The investigation area of the reconnaissance survey is located between the cities of Gera and Plauen in the Berga anticline (Fig. 2, blue box). The semi-airborne EM measurements were carried out in the region of antimony (stibnite (Sb_2S_3)) deposits near Schleiz (Fig. 2, red box). It was previously assumed that these deposits were associated with hydrothermal processes related to Silurian/Devonian magmatic activity and antimony was enriched in the Silurian rocks under certain pressure and temperature conditions (Dill, 1985). However, recent investigations have shown that antimony mineralization occurred after the late Variscan brittle deformation, probably during the Late Carboniferous (Krolop et al., 2019). Among
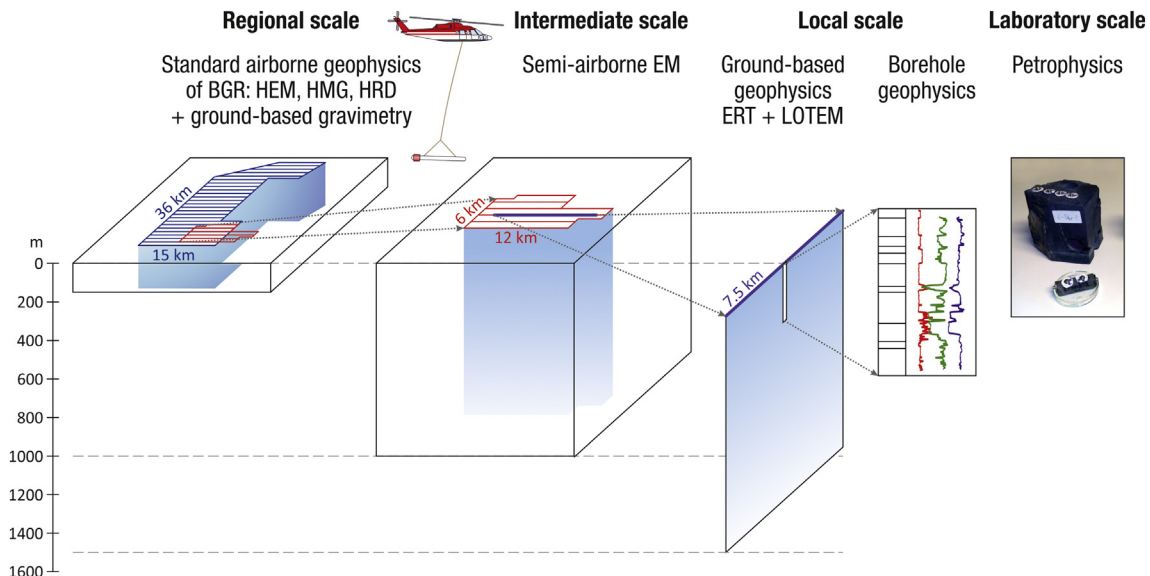

Fig. 1. Using multi-scale geophysical investigations to get an image of the subsurface in an ancient mining area in eastern Germany.
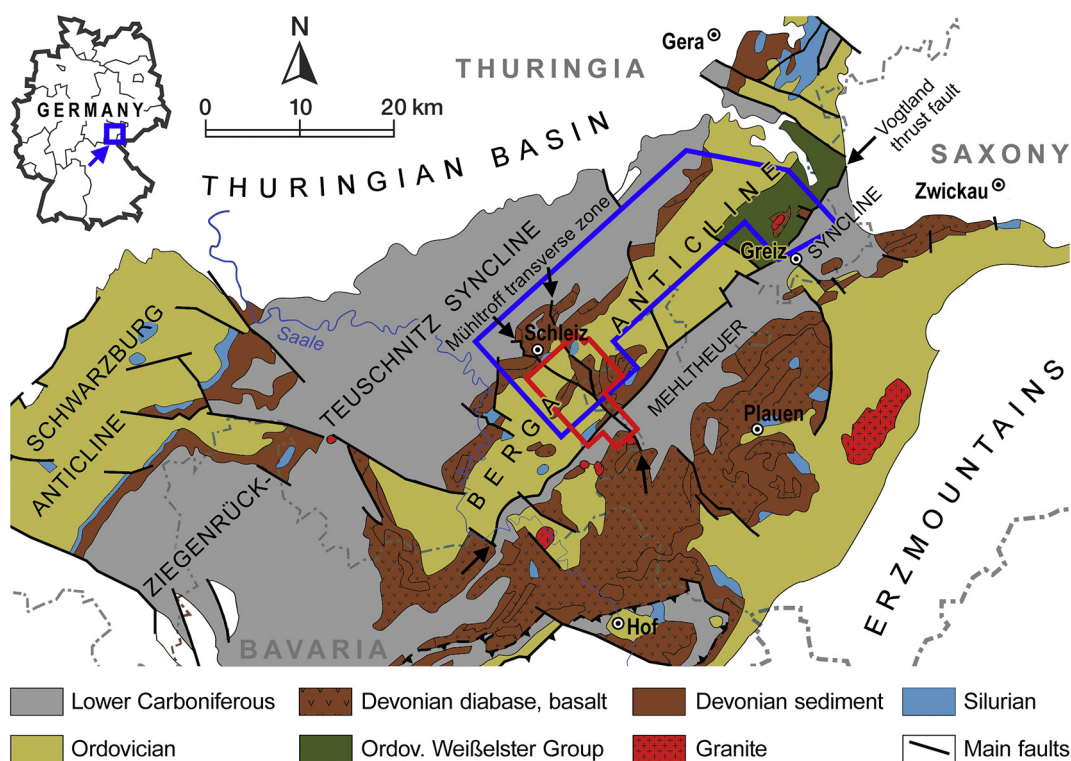
Fig. 2. Geological map (below Mesozoic and Cenozoic cover) of the Thuringian-Franconian-Saxon slate mountains (blue box on the inset map). Thick black lines indicate tectonic contacts (e.g. the Vogtland thrust fault and the Mühltroff transverse zone). The survey area of the helicopter-borne reconnaissance measurements is indicated in blue on the main map, the semi-airborne EM survey area in red. The map was edited after the geological map of Germany 1:1000000 (GK1000) (Toloczyki et al., 2006).

other mineral resources, large amounts of antimony were mined here from 1846 until the early 1950s down to depths of 200 m (Dill, 1985).

Geologically, the Berga anticline represents an antiformal structure that is elongated in the SW-NE direction. It is bordered by the Ziegen-rück-Teuschnitz syncline to the northwest and the Mehltheuer syncline to the southeast. Overall, these structures are characterized by a south-east (SE)-vergent fold architecture of conformable paleozoic strata. Due to erosion, mostly Ordovician shales and quartzites are exposed within the anticlines core. These are overlain by the thin Silurian strata (including alum shales) and Devonian strata. The adjacent synclines expose formations of the Lower Carboniferous.

Two major fault systems cross the Berga anticline. The Vogtland thrust fault in the major SW-NE fold direction dips flatly to the NW. The so-called "Mühltroff transverse zone" is a graben structure that is located in the center of the anticline and oriented almost orthogonal to it. Here, a complex system of normal NW-SE faults formed tectonic blocks and tilted the folded strata. As a consequence, younger Silurian and Devonian rocks are cropping out in this depression zone, which are elsewhere eroded in the anticlines core.

Müller and Kroner (2019) built a regional-scale 3D geological model of the Berga anticline and its tectonic sub-units based on about 200 lithological logs provided by the Thuringian State Office for Environment and Geology (TLUG). Sedimentary formations are represented in the model by their top and terrain surfaces (Fig. 3), described from oldest to youngest: an allochthonous overthrust unit from Ordovician Weißelster Group (dark green), Ordovician Phycodes (turquois) and Gräfenthal (ocher) Group, Devonian representing combined Devonian and Silurian (brown), Lower Carboniferous (gray). Due to massive diabase sill-intrusions, especially located within the Silurian and Devonian strata, and intense faulting, the stratigraphic border between those two formations is discontinuous. Thus, both strata are combined in this model for simplification. The model is divided by several faults (red

on Fig. 3), including the prominent Vogtland thrust fault from SW to NE and the system of transverse NW-SE faults.

3. Borehole geophysics and petrophysical studies

Knowledge about the petrophysical properties of the expected rocks is essential for the geophysical exploration of mineral resources to interpret the geophysical results. TLUG and Wismut GmbH (a former mining company, in 1990 the world's fourth largest producer of uranium, which is now a federal enterprise entrusted with the remediation and recultivation of abandoned mines) provided 31 borehole lithological and geophysical logs from 200 to 600 m (350 m on average) depth, which were acquired during mining activities in the 1960s and 1970s (Petrow et al., 1972). The geophysical logs include gamma-ray, resistivity and self-potential logs. The logs were scanned, digitized and interpreted. Table 1 presents the statistics of the most common lithological units occurring in the boreholes. From left to right, the lithological unit, the cumulative length of the resistivity/gamma ray-based occurrence, the 10%, 90% percentiles and the arithmetic mean (AM) of the resistivity (where AM* indicates the arithmetic mean is based on the logarithmic distribution), and the AM of the absorbed dose rate (in this case based on the normal distribution) are listed.

In addition to the historical borehole measurements, we carried out our own studies to petrophysically characterize the predominating rock types and to improve the geophysical interpretation (Costabel and Martin, 2019). These mainly comprise measurements of electrical resistivity relevant for the EM surveys, but we also measured the density and the magnetic susceptibility to support the integrated interpretation on the regional scale. Since the former mines were no longer accessible on site, we selected sample material from geological collections and additionally collected fresh samples from open pits in the area. The measured densities of most investigated rock samples (graywacke and
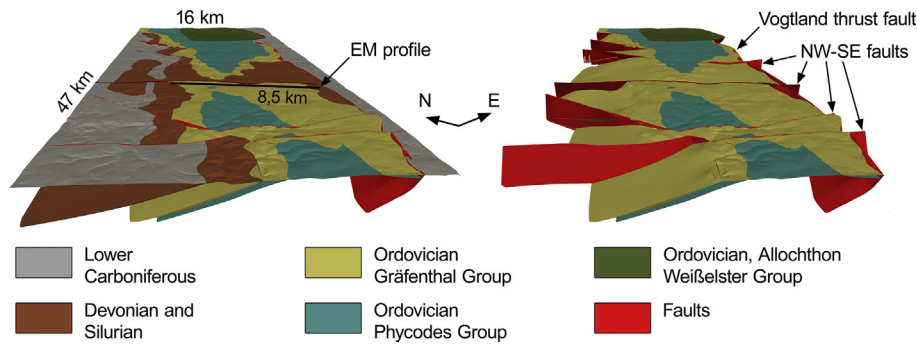
Fig. 3. 3D geological model of the Berga anticline (Müller and Kroner, 2019) represented by top and terrain surfaces of the different sedimentary formations, right-hand side without surfaces of Lower Carboniferous and Devonian/Silurian. Faults are indicated in red. The location of the EM reference profile is shown in black. It runs across the fold hinge.

shales from Lower Carboniferous; diabase, shales and quarzite from Devonian; alum shales from Silurian; shales from different Ordovician formations) vary between 2.45 and 2.93 g/cm³ and do not show systematic variations depending on the type of rock. Only the antimonite-bearing samples are characterized by high densities with more than 4 g/cm³. Furthermore, antimonite is diamagnetic (e.g. Roy et al., 1978) and exhibits a high electric resistivity, which was verified by our own corresponding measurements (Costabel and Martin, 2019). However, our surveys were not expected to identify antimonite resources directly using geophysical methods, because the antimonite deposits in the investigation area have too small dimensions (the mineral can be found only in fractured areas of fault zones). On weathered outcrop samples, we observed the highest magnetic susceptibility for diabase, with values up to 105×10^{-5} SI. The values for the diverse shale samples ranged from 7.3 to about 28.4×10^{-5} SI and show a slight correlation with the density. For many types of black shale (alum shale, graptolite shale), we measured significantly reduced values of the resistivity down to 2 Ωm (Fig. 4). Most of these samples are electrically conductive even if air-dried, which can be explained by pyrite and graphite occurrences. In contrast, the values for the other rocks present in the study area scatter unsystematically between 200 Ωm and more than 1000 Ωm.

Fig. 4 compares a part of the laboratory resistivity data (values below 10,000 Ωm) with the archival vertical electrical sounding (VES) data (Petrow et al., 1972). On average, the values measured at the field scale are smaller than those measured in boreholes or in the laboratory.

We interpret this discrepancy as a scaling effect: the larger the sensitive volume of the geoelectrical measurement, i.e., a few cm³ at the laboratory up to several hundred m³ at the field scale, the more

groundwater-filled fissures and fractures are captured, which serve as pathways for the induced currents. Correspondingly, laboratory measurements using small rock samples with almost no voids lead to the highest values, whereas the measurements at the field scale potentially include water-filled fissures and fractures. This observation has a significant consequence for the interpretation of the large-scale EM data later on. Except for the alum shales, which can exhibit resistivity values below 100 Ωm even under air-dry conditions, spatial resistivity variations in the EM models above 100 Ωm cannot be linked directly to the mineralogical or textural properties of different geological units. In the range above 100 Ωm, the resistivity values measured in our investigation area can be considered as a proxy for the degree of fracturing, weathering or metamorphism, i.e., for processes that yield an opening or closing of the water-filled pore space.

From the statistics of the archived logging data in Table 1 (Pechnig, 2019) and our petrophysical analysis (Martin et al., 2016; Costabel and Martin, 2019), we can conclude that, in terms of geophysically measureable parameters, the best distinguishable lithological units in the area of investigation are:

- Diabases – they exhibit comparatively high densities and magnetic susceptibilities. Thus, potential methods from the surface (gravimetry and magnetics) are suited for their identification. The highest resistivity and lowest gamma-ray intensity allow further identification by borehole logging.
- Alum and gravel shales – they show the lowest resistivity values and very high gamma-ray activity. Consequently, conductors in the field EM data can be clearly assigned to Silurian shales, whereas gamma-ray logs in boreholes can serve as references to verify and/or specify the field interpretation.

Nevertheless, the value ranges of the physical parameters are very wide for most rock types and the explicit correlation with only a single parameter is hardly possible. Therefore, unique identification requires a combination of multiple physical parameters, e.g., using clustering methods (Section 8.2).

4. Regional-scale helicopter-borne reconnaissance survey

The aim of the airborne reconnaissance survey, which was conducted in eastern Thuringia in 2015, was to retrieve base-line information for further investigations, such as the selection of an optimal area for the new semi-airborne EM experiments on intermediate scale.

The helicopter-borne geophysical system of BGR measures simultaneously HEM, HMG and HRD (Siemon et al., 2009; Meyer and Siemon, 2014). Navigation and positioning are based on GPS and a laser altimeter. The HEM system and the magnetometer are located in a 10 m long tube, the "bird", towed by a helicopter. The sampling interval along

Table 1

Statistical values of the petrophysical parameters over the most common lithological units in the available boreholes (Pechnig, 2019). **1 µR/h (exposure rate) equates to 9 nGy/h (absorbed dose rate). The values of the parameters, on the basis of which lithological units can best be distinguished by geophysical methods, are printed in bold.

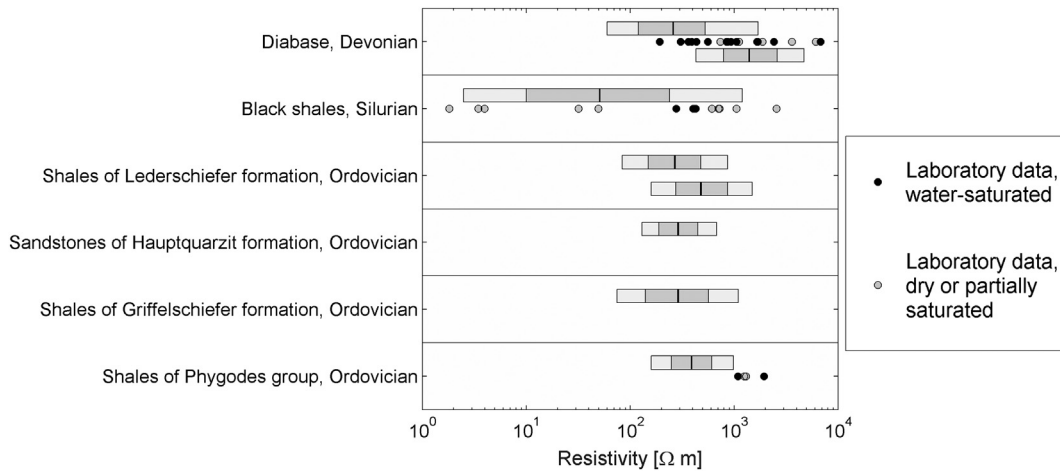| Lithology	Total sample length logged [m]	Resistivity log P10 [Ωm]	Resistivity log P90 [Ωm]	Resistivity log AM* [Ωm]	Gamma-ray log AM [µR/h**]
Diabase					
Devonian	3547/3706	111	2362	**509**	**7.7**
Clay shales					
all	2823/2982	74	937	318	18.0
Devonian	1034/1095	33	689	204	15.9
Ordovician	1653/1729	144	962	401	19.2
Alum & gravel shales					
Silurian	1319/1370	7	72	**20**	**35.4**
Carbonates					
Silurian	958/1015	25	1212	175	14.4

Fig. 4. Resistivity ranges of various relevant geological units from the study area (see Appendix A, Fig. A.1, for the lithostratigraphic table). The upper boxplot for each unit represents historical VES data and the lower one, if present, historical borehole data (Petrow et al., 1972). The dark and light gray areas in the boxplots represent the range between the 20% - 80% quantiles and the range between minimum and maximum resistivity for each distribution, respectively.

profiles is about 4 m, taking into account a survey speed of about 75.6 kn (140 km/h ≈ 39 m/s) and a sampling rate of 10 Hz. The gamma-ray spectrometer is located inside the helicopter flying at a nominal height of 70 m, while the bird is towed about 40 m below the helicopter.

An area of approximately 445 km^2 was surveyed with 124 lines and 8 tie-lines using a flight-line spacing of 300 m and 2000 m, respectively, yielding about 1600 line-km. The topographic elevation ranged from 240 to 640 m above sea level [masl]. The airborne survey required 10 flights over six days.

The HMG and HRD data were processed using standard processing steps following e.g. the recommendations of IAEA (2003) or Reeves (2005). Martin et al. (2017) describe the processing of HMG and HRD in the investigation area in detail.

4.1. Helicopter-borne electromagnetics

The HEM system RESOLVE, manufactured by Fugro Airborne Surveys (now CGG), is a frequency-domain EM system that operates at six frequencies from 387 Hz to 130 kHz to determine the resistivity distribution of the subsurface. Five horizontal coplanar (HCP) and one vertical coaxial (VCX) transmitter-receiver coil pairs are separated by about 8 and 9 m, respectively. This method enables the differentiation of e.g. salt- and freshwater (Steuer et al., 2008; Delsman et al., 2018; Siemon et al., 2019), sand and clay (e.g. Steuer et al., 2009; Siemon et al., 2015), or conductive rocks in a resistive host (e.g. Abedi et al., 2018), down to approximately 150 m depth in a resistive environment.

Careful data processing is required prior to the interpretation of inphase and quadrature HEM data for each frequency. We applied data processing techniques including zero leveling, phase corrections, calibration, elimination of data with anthropogenic noise and low-pass filtering to the survey data, described in more detail by Siemon (2006, 2009) and Siemon et al. (2011). The quality control procedures of Siemon et al. (2019) applied to the Schleiz survey indicate that the survey quality is acceptable.

A 1D inversion of the HEM data is often reasonable due to the comparatively small footprint of 120–180 m of the system (Tølbøll and Christensen, 2007; Siemon et al., 2019). The Levenberg-Marquardt iterative inversion technique (e.g. Lines and Treitel, 1984; Sengpiel and Siemon, 2000) is used for the 1D inversion, which requires a starting model. The starting models are derived individually from apparent resistivity vs. centroid depth sounding curves (Siemon, 2006). The inversion procedure stops when the decrease of the misfit (relative error of inversion in %) of field and model data between two iterations falls below a given threshold (Siemon et al., 2019).

The smooth inversion result provides resistivities and thicknesses of 20 model layers at each measurement point. This means that we receive a single 1D model every 4 m along the profile. All 1D models are stitched together to a vertical resistivity section (VRS) for each flight-line (e.g. in Section 7.1., Fig. 8b, for a part of flight-line 17.1). In this survey, we derived a total of about 375,000 1D inversion models. Overall, the mean relative misfit was 11%. In Appendix B, Fig. A.2, we show an example of field and modeled data along a part of flight-line 17.1. Beside the VRSs, the HEM inversion results are presented as resistivity maps at selected depths [meters below ground level - mbgl] by gridding the corresponding resistivities at 50 m cell size (e.g. at 30 mbgl, Fig. 5). Low resistivities are color coded in red, high resistivities in blue. The overall resistivity varies between 5 and 5000 Ωm in the surveyed area.

Based on the HEM maps, we selected an area with large variability in resistivity for the semi-airborne EM experiment (Fig. 5, red box). Geologically, the area is located in the Mühltroff transverse zone, therefore
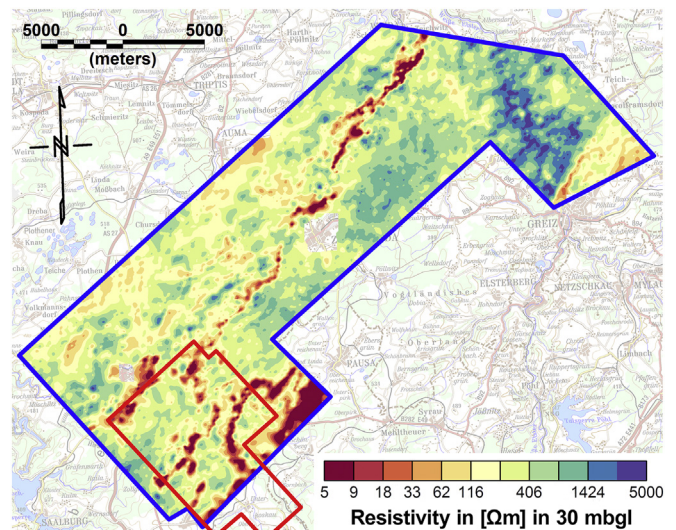

Fig. 5. Resistivity map of the HEM survey at 30 mbgl. The border of the helicopter-borne reconnaissance survey is drawn in blue, the border of the semi-airborne survey is drawn in red. Background: DTK200 (BKG, 2012).

there are large alum shale deposits (Fig. 2). In addition, antimony mining has also taken place here. From a logistical point of view, it is a suitable area for the semi-airborne EM survey, as the terrain is easily accessible for setting-up grounded transmitters and performing ERT and LOTEM surveys.

5. Intermediate-scale semi-airborne EM surveys

5.1. Concept

Our semi-airborne EM set-up (Fig. 6) used one or two grounded transmitters at a time, with dipole lengths ranging from 1 to 2 km and time varying (100% duty cycle rectangular signal) source currents $I(t)$ between 10 and 20 A, depending on the field conditions. Two different magnetic receiver sensors were installed in two bird systems, developed within the project, and operated independently.

The "induction-coil bird", designed jointly by the University of Münster (WWU), BGR, and Metronix (Braunschweig, Germany), is equipped with three induction coils MFS-11e (Metronix), a MAG-03 fluxgate magnetometer (Bartington) and a total field potassium magnetometer (GEM Systems). An MFS-11e induction coil is a compact sensor derived from broadband induction coils widely used in ground-based magnetotelluric surveys. They have an intrinsic feedback system, which yields a flat frequency response between ~100 and 10,000 Hz. In this range, the sensor output is proportional to the magnetic flux and not to the time derivative, as is often measured by the air coils used in airborne EM. We arranged three coils in an oblique setting within the airborne instrument; an orthogonal setup was not possible due to space restrictions within the casing of the bird. However, the three orthogonal components are reconstructed during the processing. Nittinger et al. (2017), Nittinger (2018) and Becken et al. (2020) presented more details on the bird design and data processing.

The "SQUID bird" was developed jointly by the Leibniz Institute of Photonic Technology (Leibniz IPHT) and Supracon AG (Jena, Germany). The instrument combines the use of new generation highly sensitive SQUID vector magnetometers introduced by Schmelz et al. (2012) with novel feedback circuits, the details of which will be published elsewhere. The successful performance of the low-temperature SQUID systems for ground-based transient electromagnetics was already shown in Chwala et al. (2011, 2013) and Rochlitz et al. (2018). The sensors used in the bird have an intrinsic noise floor of 30 fT/√Hz, the feedback enables a high dynamic range, and we observe a flat frequency response over

a broad bandwidth from DC to 100 kHz. Schiffler et al. (2014) presented the calibration and compensation of the magnetometer triplet for alignment, sensitivity, and offset errors.

Both birds are equipped with an inertial motion unit to facilitate corrections of motional noise and rotation of the data to an earth-fixed coordinate system.

5.2. Surveys

Two semi-airborne EM surveys were conducted in the Schleiz area, one in 2016 and one in 2017. During the first test survey in 2016, three flights were performed over three different transmitter installations. The flights covered an area of about 35 km² using a flight-line spacing of 100 m near the sources and 300 m towards the periphery of the survey area. The area of the 2016 survey covers approximately the sub-area A1 of the 2017 survey (Fig. 7, pink dashed box). Smirnova et al. (2019) described the survey and the resulting 3D inversion model in detail. During the second survey in 2017, an area of about 74 km² was covered with a line spacing of 250 m (Fig. 7, red box). The region was separated into eight overlapping sub-areas A1-A8 each of 6 × 3 km² extent. In each sub-area, two transmitters separated by about 1–2 km (e.g. Tx1 and Tx2 in sub-area A1, cf. Fig. 7) were operated simultaneously but at different fundamental frequencies. As an exception sub-area A7 contained only a single transmitter (Tx14, purple dashed box in Fig. 7). The objective of using two independent transmitters for a single flight was to increase the efficiency of the survey. The transmitters operated at different fundamental frequencies (7.6 and 10.4 Hz), allowing signal separation of the fundamental frequency and many of the harmonics in the spectral range. Petersen et al. (2018) provided a detailed description of the survey.

The processing procedure for the data of both birds requires two main steps: (1) removal of the motional noise from the data and rotation of the data to a geographic coordinate system, and (2), processing of the data in the frequency domain to estimate transfer functions between the field components and the source current (Schiffler et al.,
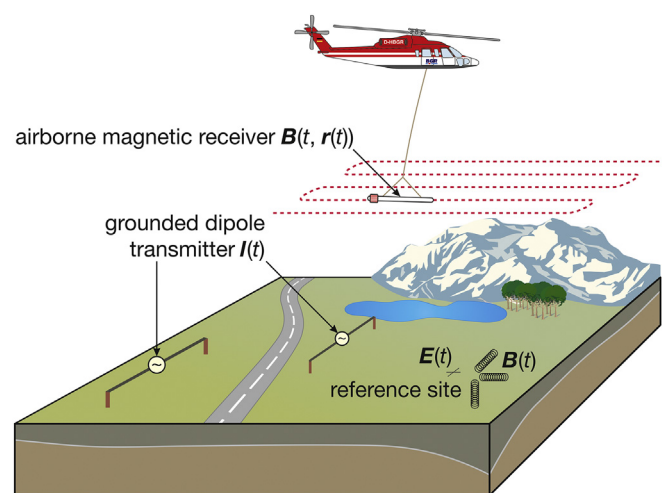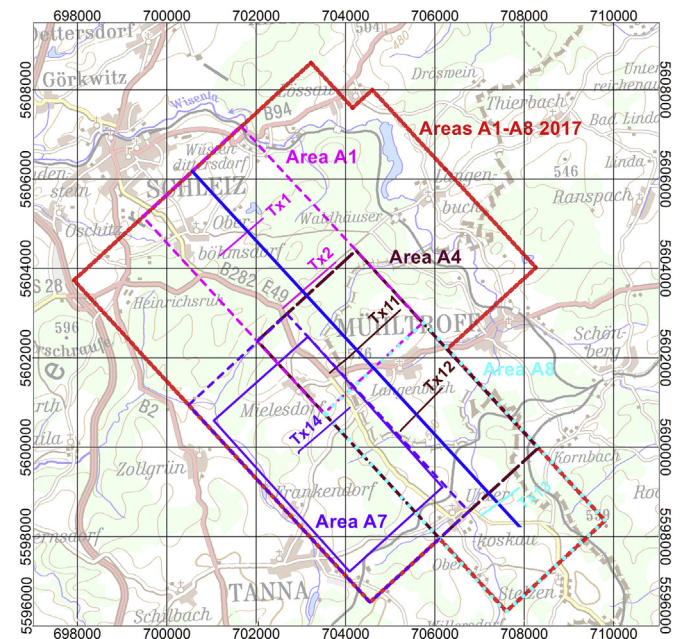

Fig. 6. Semi-airborne EM method with large-scale dipole transmitters $I(t)$ on the ground, and airborne receivers towed by a helicopter detecting the magnetic field $B(t, r(t))$ where $r(t)$ is the location. At a reference site, electric and magnetic fields, $E(t)$ and $B(t)$, are measured by ground-based receivers.

Fig. 7. Location of some of the overlapping semi-airborne survey sub-areas (colored dashed boxes) with their corresponding transmitters Tx1-Tx14 in the associated color. The external border of all sub-areas A1-A8 (surveyed in 2017) is drawn in red. A blue line indicates the location of the reference profile and the purple solid box the location of the 3D model. Background: DTK200 (BKG, 2012).

2014; Nittinger et al., 2017; Nittinger, 2018; Smirnova et al., 2019; Becken et al., 2020).

Next, we delineate firstly a 2.5D inversion of induction-coil data obtained from a total of five transmitters along a merged flight-line which was performed for the comparison with the ground-based profiles and, secondly, a 3D inversion of SQUID data in sub-area A7 obtained from a single transmitter. Note that these two examples are independent realizations of the semi-airborne EM method using different instruments, different processing codes and different inversion codes.

5.3. 2.5D inversion

We performed the 2.5D inversion (3D source and 2D model) on induction-coil data from the overlapping flight-lines 107, 407 and 807 (Section 7.1., Fig. 8a), which are located nearby HEM flight-line 17.1. For this inversion, transfer functions were rotated into a coordinate system aligned with the flight-line and the horizontal component in flight direction (perpendicular to the transmitters allowing a 2D analysis) was jointly inverted with the vertical component. The observed data included these two components from a total of five independent transmitters and for frequencies ranging from 10 to 4000 Hz. Careful data selection was performed for each component, frequency, and transmitter separately, to eliminate obviously noisy estimates. In total, about 18,000 data points were gathered for inversion. The jointly inverted

quantities comprised the logarithm of the amplitude and the phase of the transfer functions. The inversion seeks a trade-off between data residuals and model roughness in the sense of the well-known Occam inversion scheme (de Groot-Hedlin and Constable, 1990). The data misfit measure is weighted by the data errors to avoid overfitting of the data. Too small estimation errors in subsets of the data can lead to biased inversion results. Therefore, in addition to the estimation errors, error floors were imposed on the data. It means that at best we aimed at fitting the data to within these error floors. An error floor corresponding to 5% in linear data space was assigned to the amplitudes and a constant error floor of 5° on the phases were found to result in an overall good fit of all data components.

The inversion was carried out with the Mare2DEM code (Key and Ovall, 2011), which allows for the calculation of field response for an extended dipole source and a 2D conductivity distribution. We chose a 100 Ωm half-space as the starting model, which included the topography below the flight-lines. Observational points were modeled at the actual flight height above the surface. Multiple inversion tests were run with varying inversion parameters and varying data combinations, including separate inversions for each transmitter. The final inversion model (Section 7.1., Fig. 8c) achieved a target (error-weighted) root mean square error (RMS) of 1.5 after 12 iterations, followed by 3 iterations of the second inversion stage aiming at reducing the model norm while maintaining the target misfit. The RMS measures the sum of
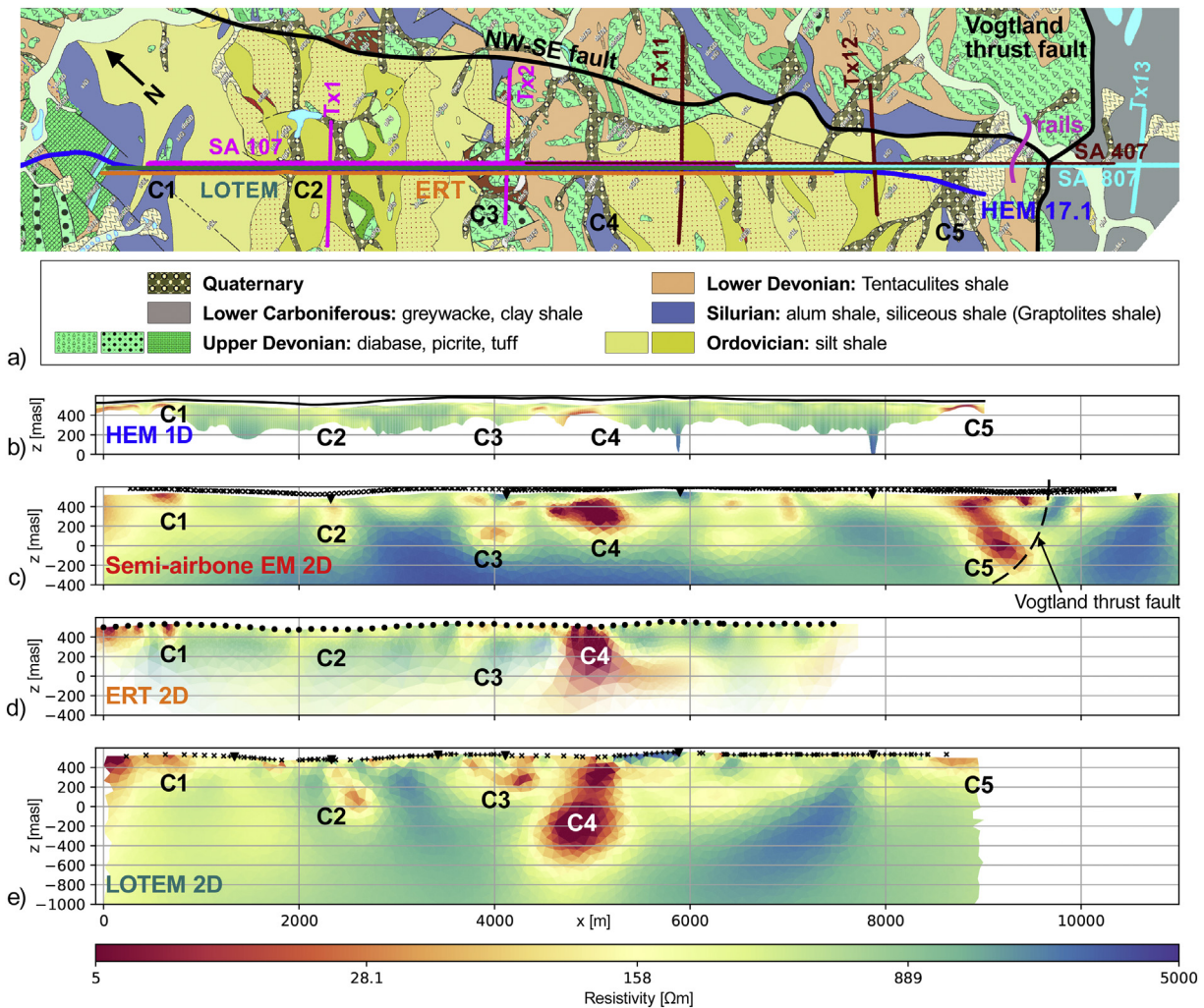

Fig. 8. a) Geolocial map (GK25dig Th) with the locations of the flight-lines/profiles, semi-airborne EM transmitters (Tx1-Tx13) and conductive anomalies (C1-C5). b) HEM 1D inversion results at flight-line 17.1. c) Result of the 2D inversion of the semi-airborne induction-coil data at the overlapping flight-lines 107, 407, and partly 807. d) ERT 2D inversion result. e) LOTEM 2D model of the joint inversion of E_x, B_z and B_y. b)-e) The measuring points are marked by points or crosses, the transmitter positions of LOTEM and semi-airborne EM by triangles.

squared distances of the observed and predicted data normalized by the larger of the estimated data variances, or the imposed error floor. An RMS of 1 thus means that the data are fitted by the model within the error. An RMS of 1.5 indicates that the data are well fitted and the estimation errors in combination with chosen error floors are of reasonable size. We show an example of the data fit in Appendix B, Fig. A.3.

5.4. 3D inversion

The geological map revealed structures that require the 3D interpretation of a complete semi-airborne data set (not only one flight-line). Therefore, we provide an example of a 3D inversion on SQUID data collected over sub-area A7 using one transmitter T14 in the center of the sub-area (Fig. 7). The SQUID data were processed using the KMSProMT software (Smirnov, 2003) in a similar manner to that described by Smirnova et al. (2019) for the induction-coil data. In total, we used data (vertical magnetic component of the transfer function $TF = B_z/I$) from 406 receiver positions along NW-SE flight-lines at eight frequencies from 30 to 1096 Hz. We show a plan view of the TF for two frequencies in Appendix B, Fig. A.4.

Prior to the inversion, the data were controlled for the spatial consistency of the TF estimations and their smooth behavior with frequency. If certain data could not be fit during 3D inversion (exhibit high RMS fit), they were removed from subsequent inversion trials. The modelling domain was uniformly discretized into $77 \times 115 \times 55$ cells, with a horizontal cell size of 50 m and a minimum vertical cell size of 20 m. The starting model was a half-space with a resistivity of 200 Ωm. The selection of resistivity values for a starting model is based on the HEM models, where background resistivity varies around 100–300 Ωm. Several values were tested. The data were inverted using the 3DINV algorithm (Grayver et al., 2013). A Gauss-Newton optimization technique was used for the inversion, with a starting regularization parameter of 0.1. Several values of the starting regularization parameter were tested; the value 0.1 provides the best convergence rates. The inversion converged to an error-weighted RMS of 5.5 after 11 iterations, starting from an RMS of 23.0. We used estimated random data errors and an additional error floor of 2% to avoid overfitting of the data. The resulting resistivity values ranged from 1.2 to 8600 Ωm (Section 7.2., Fig. 9). We show an example of field and modeled data along a flight-line in Appendix B, Fig. A.5.

6. Local-scale ground-based surveys

6.1. Large-scale ERT

Electrical resistivity tomography (ERT), often called only resistivity in the context of mining, is a method widely used for resistivity mapping or sounding to investigate a range of geological and hydrogeological problems. The typical experimental layouts in near-surface investigations use multi-electrode instruments with up to a few hundred electrodes with electrode spacings between 1 and 10 m on 2D profiles, reaching penetration depths of about 100 m. It is common in mining and for other investigation purposes, to use larger electrode spacings of about 100 m to reach significantly deeper penetration depths. We used the equipment as reported by Nickschick et al. (2019), consisting of separate metal-rod injection electrodes and non-polarizable Ag/AgCl receiver electrodes. The current source, developed at LIAG, transmitted a low-frequency (0.2 Hz) 100% duty cycle current of up to 50 A, providing a very good signal-to-noise level. Oppermann and Günther (2018) described the three-channel data logger used for the receivers in this survey and the data processing steps.

A section of 7.5 km length was measured in dipole-dipole configuration (105 m dipole length) with maximum dipole spacings of 3.5 km in two separate campaigns, carried out in the autumn of 2015 and 2016. An investigation depth of about 500–700 m was reached. The traverse coincided with the other traverses (orange line in Fig. 8a, Section 7). The data quality was very good up to the largest electrode separations as indicated by the reciprocity ratio, which showed only differences between the different injection and receiver electrode types (Oppermann and Günther, 2018). The inversion was conducted with the BERT 2D inversion software (Günther et al., 2006), which is based on irregular triangular meshes taking the correct topography into account. After 12 iterations the data fit reached a value of 24.2% (Appendix B, Fig. A.6), which is rather high, but acceptable in view of the extreme range of inverted resistivity values between 1 and 5000 Ωm (Section 7.1., Fig. 8d).

6.2. LOTEM

The long-offset transient electromagnetic (LOTEM) method is an active ground-based EM method that uses, similar to the semi-airborne
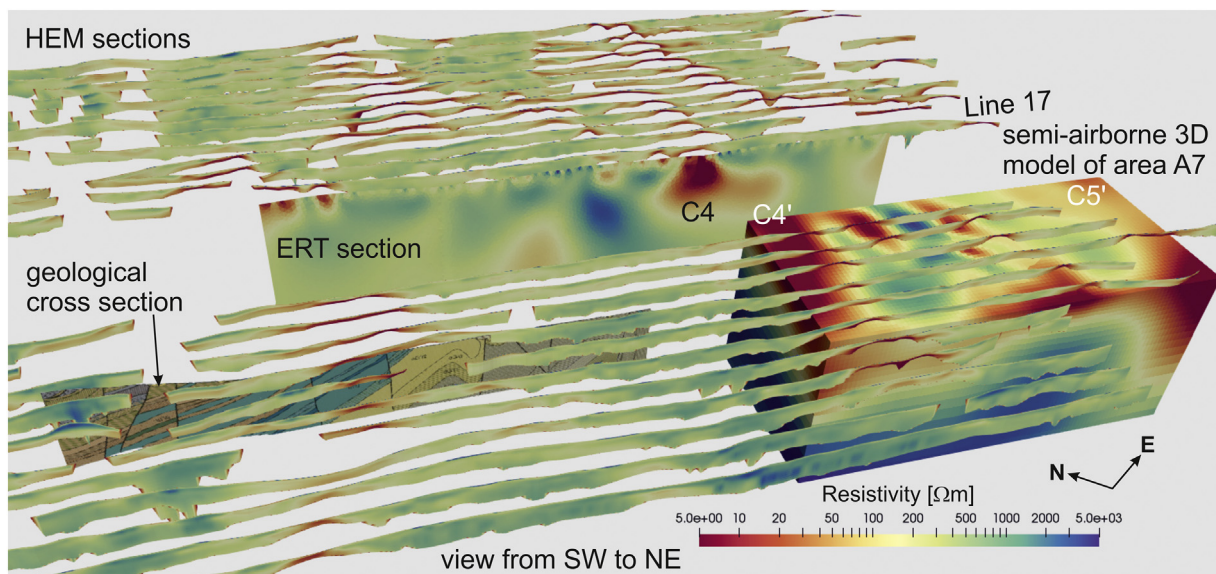

Fig. 9. Perspective view of a part of the HEM sections together with the semi-airborne EM 3D inversion model of sub-area A7 on the right side and the ERT section in between. Discussed conductive anomalies are indexed with C. A geological cross-section with the submerged layers of the Silurian alum shales (turquoise color) is also shown.

EM approach, a galvanically coupled electrical dipole, transmitting a 50% duty cycle source signal with low base frequencies between 0.25 and 0.56 Hz. Measuring the transient response of both, the electric and magnetic fields, at offsets of several km, the method is typically applied to retrieve information about deep targets down to a few km (Strack, 1992).

During the DESMEX surveys in 2016 and 2017, six LOTEM transmitter positions were set up with their bipoles in the same direction as the regional geological strike direction (SW-NE, x-direction), with current amplitudes between 10 and 24 A and transmitter lengths of about 1 km. Ground-based data of the electrical field (E_x) as well as horizontal and vertical magnetic field data (B_x, B_y, and B_z), utilizing SQUID sensors (Leibniz IPHT), were acquired. Receivers are located along the 8.5 km long validation profile, recording from multiple transmitter locations within offsets ranging between 500 m and up to 5 km. The high-power and fast-switching device GGT 30 from ZONGE was utilized as transmitter, the KMS 820 units (KMS technologies), the SPAM Mk 4 (geophysical instrument pool Potsdam GIPP) and the SMARTem device (EMIT) served as receivers. The recorded dataset exhibited a good data quality over the entire time range from 0.1 ms to 1 s or for frequencies (signals converted to frequency domain) between 1 Hz and 1 to max. 10 kHz, respectively. More details about the survey setup, the processing schemes and the dataset are provided by Mörbe et al. (2020).

Due to the complex geology in the survey area and the large footprint of the LOTEM method, the dataset cannot be reasonably analyzed with a 1D inversion approach. For a multi-dimensional interpretation, the LOTEM data was transferred into frequency domain. A 2.5D inversion was conducted using the finite-element code Mare2DEM (Key and Ovall, 2011), including frequencies between 1 and 1000 Hz. For inversion, extensive parameter studies were carried out, including different starting parameters, error settings, smoothing constraints and single component inversion (Mörbe, 2020). Strong outliers were excluded from subsequent inversion. An error floor corresponding to 5% in linear data space was assigned to the amplitudes and a constant error floor of 2° to the phases to all components for inversion. In the final model, in total 16,400 data points, including the broad-side electrical-field component, the magnetic-field component along the profile direction (y-direction) and the vertical magnetic component, were inverted jointly. As the starting model, a homogeneous half-space of 300 Ωm was used. The joint inversion (Fig. 8e) reached after 12 iterations an error-weighted RMS of 4.9. Deviations from an optimal fit of 1 are most likely due to induced polarization and 3D effects, which are not accounted for in the inversion and in addition affect electric and magnetic field components differently. In Appendix B, Fig. A.7, we show an example of field data and modeled data along the profile. As discussed by Mörbe (2020), the model exhibits a high sensitivity towards conductive structures within the validation depth up to 1 km.

7. Multi-scale EM results and interpretation

The different EM methods have their specific application due to their respective depth of investigation, spatial resolution, data coverage, and their adequate size of a survey area ranging from regional to local scale. The investigation depths partly overlap and complement each other. Similarly, the resolution capabilities with respect to the recorded EM field components complement each other. In the following, we first use the overlapping investigation depths to verify the resistivity model of the newly developed semi-airborne EM method along one transect. We interpret the 2D resistivity models with the help of the geological map and under consideration of the petrophysical information. Secondly, a 3D inversion result of one of the sub-areas demonstrates the ability of the semi-airborne EM method to investigate the conductivity structures of the subsurface down to a depth of roughly 1000 m on an intermediate scale, covering a significantly larger area than 2D transects could. We present the 3D resistivity model together with the resistivity models of the other methods to illustrate the different scales.

7.1. Verification of the semi-airborne EM

Fig. 8a shows the overlapping profiles of the different EM methods on the geological map. The HEM flight-line slightly bends to the south at the SE end. Fig. 8b to e illustrate inversion results, starting with the stitched HEM 1D models, followed by the semi-airborne EM, ERT, and LOTEM 2D models. The resistivity of all methods varies mainly between 5 and 5000 Ωm. Low resistivities are color coded in red, high resistivities in blue. We assigned labels to the prominent electrical conductivity anomalies from left to right (C1-C5). A dashed line indicates the northwestwards dipping Vogtland thrust fault from the 3D geological model (Müller and Kroner, 2019) overlain on the semi-airborne EM 2D model.

The HEM results revealed the resistivity down to about 150 m depth (Fig. 8b). At sites with a conductive subsurface, the model depth was reduced significantly to only 70 m depth. The semi-airborne EM 2D model (Fig. 8c) and the ERT model (Fig. 8d) exhibited a much deeper investigation depth of at least 50 m, whereas the LOTEM model (Fig. 8e) provided even deeper resistivity information down to 1000 m. The nearest available borehole logs are more than 600 m away from our section and are therefore of limited use for the interpretation and validation of the 2D resistivity sections.

The models display an overall resistive subsurface with intermediate values of 300–1000 Ωm. In addition, there are several conductors (C1-C5) with resistivities below 10 Ωm visible in all models, one (C1) at the beginning of the profile, one (C4) at about 5000 m, and one (C5) at 9000 m profile distance. We can clearly attribute them to the occurrences of alum shale (partly covered with solifluidale Quaternary deposits). This assessment is supported by our laboratory investigations, which have identified resistivities below 100 Ωm only for black shales (see Fig. 4). C1 is divided in two parts (according to the geological map) and reaches depths of at least 250 m. Unfortunately, the zone at the end of the semi-airbone EM line is not well resolved. C4 is dipping southeastwards in the upper 250 m. It is clearly visible in the semi-airborne EM and ERT models and varied northwestwards at depth in the ERT and LOTEM results, reaching depths of about 500 m (semi-airborne EM), potentially even 1000 m (ERT and LOTEM). However, the resolution of the lateral and depth extension of the conductor decreases with increasing depth. Furthermore, the high conductivities at greater depth can also be a result of an anisotropic behavior of C4 of the upper few hundred meters (Liu et al., 2020). C5 is indicated at the end of the semi-airborne EM section, but not covered by the ERT measurements. In contrast, the LOTEM model was able to partially map the anomaly C5, but could not support tracing C5 to depth due to the lack of data coverage at the SE edge of the profile. Only the semi-airborne EM measurements extended far beyond the southeastwards dipping anomaly C5. It seems very reasonable that this anomaly reaches more than 500 m depth, limited by the northwestwards dipping Vogtland thrust fault. Regarding the top of the Ordovician Gräfenthal Group in the 3D geological model (Fig. 3), on which the Silurian alum slates were deposited, the dipping of C5 to the southeast is reasonable. According to the geological map, the anomalies C1, C3, C4 and C5 were interpreted as depressional zones of the complex graben structure of the Mühltroff transverse zone (see Section 2 above). Aside from the significant conductors, several features with even high resistivity (>1000 Ωm) are visible, e.g. between C2 and C3 and between C4 and C5. According to the geological map and the 3D geological model, these resistive structures might be interpreted as Ordovician clay and silt shales at the near surface and at greater depths as Ordovician phyllites and quartzites. With respect to the preliminary petrophysical results (Section 3), we concluded that higher resistivities indicate processes that have less water-filled pore space, e.g. unweathered or metamorphosed rock.

7.2. 3D view of multi-scale EM models

The perspective view of the multi-scale EM models in Fig. 9 illustrates the different spatial and depth scales of the methods. In addition to the semi-airborne EM 3D model of sub-area A7 (about 13.5 km² of a total of 35 km² and 1000 m deep), Fig. 9 shows 30 (of the 124) NW-SE HEM sections (about 70 km² of a total of 445 km² and about 150 m deep), the ERT section (7.5 km long and about 1000 m deep), and a geological cross-section. A comparison of the 3D model with the HEM sections illustrates the good agreement of the alternating resistivity structure in the near-surface region of the 3D model. The conductive structure C4 of the ERT 2D section continues in the 3D model (C4′). The depth of C4 and C4′ is comparable in both models. Also, the conductive structure C5 at the border to the Vogtland thrust fault continues in the 3D model (C5′). Fig. 9 shows that the assumption of the main strike direction justified the 2D inversions. However, there are also very clear 3D structures that require a final 3D analysis of the deep EM and ERT data. A direct correlation of the 3D semi-airborne EM model with the HEM map and the geological map is shown in Section 8.2, Fig. 12, when compared with the results of the cluster analysis.

8. Multi-parameter results and interpretation

The petrophysical parameters of the investigated geological units prevailing in the study area span a wide range for most rock types (Section 3, Table 1 and Fig. 4). An explicit correlation with only a single parameter (such as the electrical resistivity) is hardly possible. The regional-scale airborne geophysical survey provided spatially dense data from multiple techniques that are sensitive to various physical parameters. This offers great potential for an integrated interpretation. In the following, we used statistical methods to identify geological units and compared these to our deep EM results.

8.1. Results of the regional-scale geophysical methods

The regional scale helicopter-borne geophysical survey provided HEM, HMG and HRD data. In our statistical approach, we also used ground-based gravimetric data from a countrywide gravimetric mapping.

We have used the HEM method to obtain a large-scale overview of the electrical resistivity distribution of the subsurface at depths down to 150 m in the study area. Comparing the resistivity map and the geological map (Fig. 10a and b), most of the conductors with resistivities below 10 Ωm correlate with outcrops of Silurian alum shales (Graptolite shale). Strong variation and conductive outcrops are visible within the flight-area of the semi-airborne EM experiment. However, the correlation of alum shales to conductors is visible for the entire regional scale flight-area (Fig. 11a and f).

Due to the complex geology, we have not modeled the magnetic data and therefore only provide the map of the analytic signal of the magnetic field anomalies, which range from 0 to 0.2 nT/m. Strong magnetic anomalies (red) occur at the places with diabase (Fig. 11b and f) and indicate thick diabase occurrences at depth. This visual interpretation is supported by the laboratory studies that measured the highest magnetic susceptibilities for diabase (Section 3).

Moreover, we present radiometric results in the form of the total-count map (Fig. 11c), which range from about 400 to 1300 cps. Regions with medium gamma radiation (orange) are correlated with clay shales of the Ordovician and Lower Carboniferous, regions with strong gamma radiation (red) with phyllites of the Ordovician Weißelster Group, and regions of low gamma radiation (blue) with outcrops of diabase (Fig. 11c and f). The delineation of the expected strongly radiating Silurian alum shales is diffuse in the total-count map. From the ternary representation (Martin et al., 2017) it can be seen that the phyllites show a slightly potassium accentuated signature, in contrast to the Silurian, which is strongly uranium accentuated. According to Meinhold et al.

(2005), the phyllites in the core complex of the anticline all show a felsic provenance. Felsic magmatites usually have a high ^{40}K activity, which might explain the K-emphasized signature of the radiometrics (Fig. 11c, black dashed circle). The adjacent metasediments to the southeast are rather mafic in their provenance and are well delimited in the radiometrics. Furthermore there are some small granitoid intrusions in the phyllite complex which could also contribute to the increased radiation.

The resolution of the gravity data (LIAG, 2010; Skiba, 2011) in our area was not sufficient to obtain a good estimate of possible sources, such as mineral deposits and/or surrounding volcanic/plutonic outcrops. However, it was possible to obtain some evidence of a deeper signal (large wave-number signal), which we could relate to the folding of the granulite basement on a regional scale, aligned with the axis of the Berga anticline (Zampa, 2019). The residual field obtained from band-pass filtering operations (Butterworth filter with 15 km to 2 km cut-off wavelength) (Fig. 11d) appears to be related with some geological structures, suggesting the uplift of denser plutonic/volcanic outcrops. Moreover, the filtered signal highlights the presence of granitic formations (medium to late Devonian meta-granitoids, according to the geological map GK25dig Th) correlating spatially to the relative negative minima of the gravity data (Fig. 11d, black dashed circle).

8.2. Integrated interpretation using self-organizing maps

The combination of the different measurement and mapping methods can provide a comprehensive picture of the subsurface. So far, we analyzed the particular geophysical models independently and used visual comparisons to identify similar clusters. In addition, similar classes can be recognized by integrating several parameters into a map. The developed approach uses statistical methods such as clustering and self-organizing maps (SOMs) to detect patterns in the distributions of resistivity, magnetic susceptibility, gamma radiation and gravity (Preugschat, 2020).

The SOM algorithm (Kohonen, 2001) belongs to the unsupervised learning algorithms of deep learning. The use of the SOMs allows the objective comparison of data on different scales with each other. Clusters are the result of the comparison. Each cluster represents an area with similar geophysical properties. The assumption is that these areas with the same geophysical properties correspond to geological units. A unique classification of the clusters is expected from the results from the boreholes and the petrophysical measurements, which we used to calibrate the model.

The first step of the SOM data processing is the creation of a feature table. Here, the table consists of HEM, HMG, HRD and gravimetry data. In the next step, visual examinations and data normalizations were performed for all features after removing data outliers. We conducted feature tests on the corrected feature table to make a selection. With the selected features, we could define data subsets, which we used for the cluster analysis with the SOM algorithm. Finally, we applied validation tests to the clustered maps. For the classification of the clusters in the maps, the measurements of borehole data and petrophysical data were compared using a minimum distance approach. The principle of the developed clustering approach is illustrated in Appendix C, Fig. A.8, and described in more detail by Preugschat (2020).

The result of a cluster analysis with the SOM algorithm is visualized in Fig. 11e and reveals the distribution of the clustered geophysical properties in the investigation area. The used subset contains the resistivity at 30 mbgl, the filtered magnetic analytic signal, the concentration of potassium, the equivalent concentrations of uranium and thorium, and the residual anomaly of the gravity data. It was possible to determine seven different stable clusters. By comparing the clusters with the geological map (Fig. 11e and f), it was possible to find correlations between clusters and lithological units based on their shapes and positions:
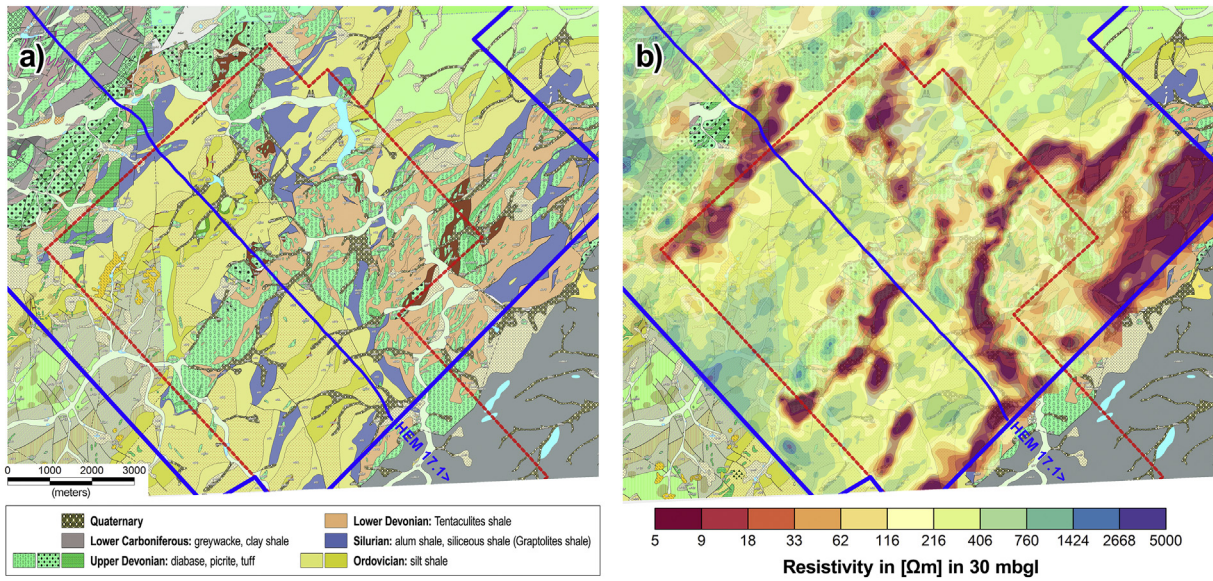
Fig. 10. a) Geological map of Thuringia (GK25dig Th, Gräbe et al., 1996, Liebe et al., 1912). b) Resistivity map (on top of the geological map) of the HEM survey at 20–30 mbgl. The external borders of the helicopter-borne reconnaissance survey and of the semi-airborne EM surveys (2017) are drawn in blue and red, respectively. The blue line indicates the HEM flight-line 17.1.

➢ Cluster 1: alum shale of the Silurian;
➢ Cluster 2: graywacke of the Lower Carboniferous;
➢ Cluster 3: clay shale and graywacke of the Lower Carboniferous;
➢ Cluster 4: quartzite/phyllite of the Ordovician Weißelster Group;
➢ Cluster 5 and 6: clay and silt shales of the Ordivician Gräfenthal and Phycodes Group;
➢ Cluster 7: diabase.

The visual comparison also confirmed the calculated classification (Preugschat, 2020).

In the following, we look at this in detail using the example of sub-area A7 in order to compare the SOM results with the shallow resistivity maps based on the HEM and semi-airborne EM data (Fig. 12).

Again, the correlation of Cluster 1 with the Silurian alum shales (C4´-C7´) is very clear. In the visual comparison on this intermediate scale, Cluster 2 could be assigned to the Ordovician Gräfenthal Group, whereas on a regional scale Cluster 2 seems to be clearly assigned to the Lower Carboniferous. The interpretation of the clusters is therefore not unique. Nevertheless, more geological units can be identified by the application of SOMs than by the resistivity models alone, e.g. Upper Devonian diabase can be clearly distinguished from Ordovician clay shales (Fig. 12 a and b). A resistivity map of the HEM was chosen as representative of the EM methods for the preparation of the SOMs, as the large area covered by the HEM provides the best statistics for the SOMs. Since the resistivity maps of HEM and semi-airborne EM are very similar in the near-surface region of our study area (Fig. 12 c and d), it can be assumed that a similar SOM would be obtained with the semi-airborne EM map.

9. Discussion

9.1. EM results

EM inversion is generally a non-linear problem with respect to model parameters. Firstly, we employed different codes for the inversion of the data, and each method used an independent model parameterization and field discretization imparting on the regularization term. Secondly, we have to account for the fact that different data types (with different resolution) were inverted. For the semi-airborne EM inversion,

and for the HEM inversion, only magnetic components were used. The magnetic components of the EM fields in the air are poloidal fields (or tangential electric, TE-mode) and primarily respond to zones of current concentration. DC data, in contrast, is a galvanic and not an inductive method. The LOTEM method used electric field recordings in a broad side configuration. However, when the geometry is not perfect or when the subsurface is not strictly 2D, the broadside measurements are afflicted by both EM modes, the TE and the tangential magnetic (TM) mode. Hence, galvanic and induction currents become relevant. Therefore, the sensitivity of the different methods to conductors and resistors is different. Thirdly, the model assumption is limited (2D vs. 3D), and IP effects (and electrical anisotropy) were not admitted. However, they were taken into account by the errors floors. Hence, even in case of perfect data, the EM inversions cannot be expected to yield identical results when using different data and different codes. For these reasons, e.g., the conductive body C4, varies in the presented inversion results. Nevertheless, the different models compare well overall.

To further demonstrate the applicability of the semi-airborne EM method with our measurement systems, an industrially relevant deposit, the Kiruna iron ore deposit in North-Sweden, was investigated in another measuring campaign in 2018. Smirnova et al. (2020) present the first results.

9.2. Clustering

The assignment of clusters to geological units can be a challenge. In general, errors can occur during the clustering or the classification. The following factors and assumptions, which will be discussed briefly, are decisive in this context.

The main cause of the supposedly faulty clustering is based on selection of the feature data. While resistivity data from electromagnetics were available as 3D data sets, the data from magnetics, gravimetry and radiometrics were only available in 2D maps. We used the resistivity map from 30 mbgl to ensure that the resistivity is represented by the solid rock. From the data of magnetics and gravimetry the long-wave components were filtered out. Thus, the results represent the upper 100 m of the investigation area. An exact depth allocation was not possible due to a missing 3D inversion of the data. Radiometrics has only a few decimeters of penetration depth. In the study area, the solid rock is
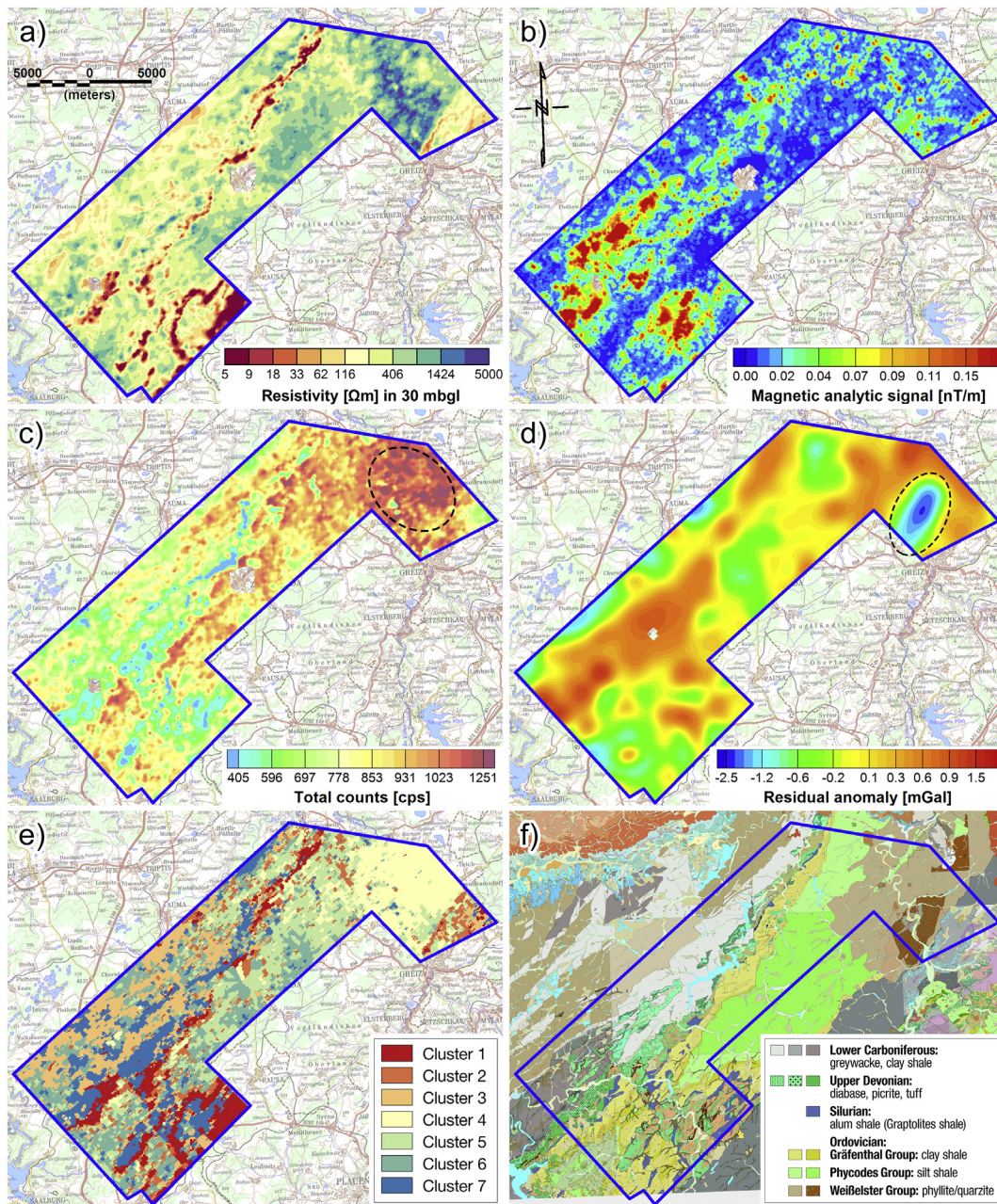
Fig. 11. Regional scale: a) Resistivity map of the HEM survey at 30 mbgl, b) Magnetic analytic signal of the HMG survey, c) Total counts of the HRD survey, d) Residual anomaly map of ground-based high-pass filtered gravity data (Zampa, 2019), e) Result of the cluster analysis with SOMs. f) Geological map of Thuringia (GK25dig Th, Gräbe et al., 1996, Liebe et al., 1912). Background: DTK200 (BKG, 2012).

usually close to the surface. Assuming that in-situ weathering without major redistribution took place, the radiometric data directly reflect the solid rock properties. The geological strata are relatively steep in the study area. This makes it possible to compare the data of the different methods on the basis of SOMs despite the different depths of investigation. A second source of misinterpretation is the different sampling density of the data. The unification through interpolation necessary for the clustering can lead to the suppression of structures, but also to smearing of structures. Parameters with lower data density (here, for example, gravity) can therefore blur the boundaries of clusters. The overlapping of the boundaries of the clusters can also be caused by the large value ranges of the parameters for most of the rock types (Section 3). As a result, the data from two or more clusters may not be clearly separated and may be randomly assigned to one cluster.

The classification in our case, was determined based on a few data from petrophysics and the borehole-data. Initial in-depth testing was promising and further elaboration on this topic will be carried out in the future. To improve the statistics here, larger data sets are necessary.

For these reasons, the interpretation of the clusters is not always unique in our study area. Nevertheless, more geological units could be identified by the application of SOMs than by the resistivity models alone.

The two-dimensional approach of the SOM method used here can be extended to 3D to further support the synthesis of resistivity, petrophysical and geological data. For a promising application, 3D models of various physical parameters, e.g. resistivity, density and magnetic susceptibility, must then be available. Here we could take advantage of data from different scales. High-resolution regional-scale data
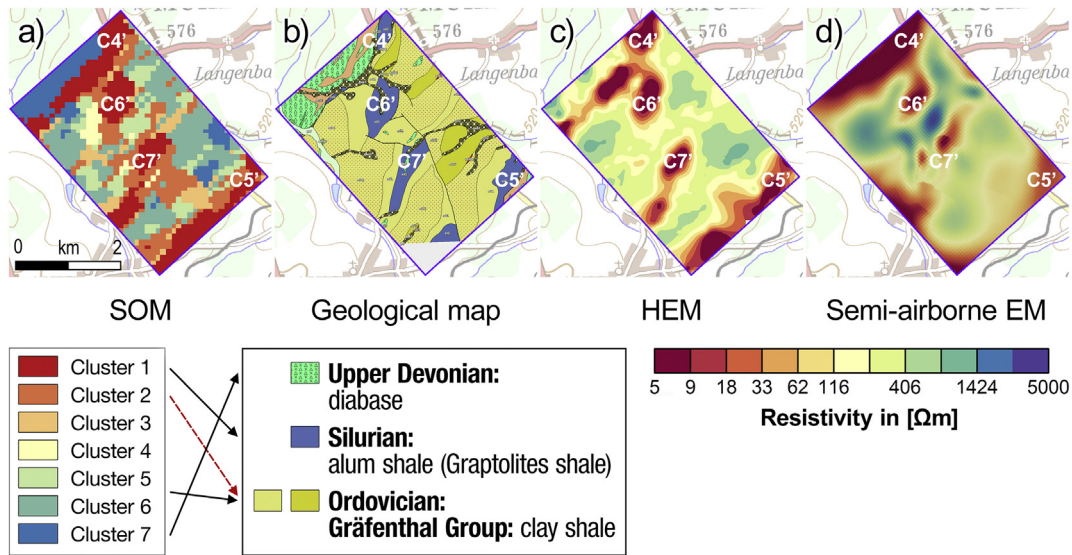
Fig. 12. Sub-area A7 with conductive anomalies (C4′-C7′): a) SOM, b) geological map, c) HEM model at 30 mbgl, and d) semi-airborne EM 3D model at 50 mbgl. Background: DTK200 (BKG, 2012).

improve the clustering and many petrophysical investigations (on samples from open pits or borehole logs) are important for the classification. The data set from the SOM clusterings can be used to train and test an artificial neural network (ANN) with supervised learning algorithm. The trained and tested ANN can then be applied to the deeper model space with the semi-airborne data on the intermediate scale. Thus, these data can also be classified geologically and structurally without the need of new clustering. In this way, similarly well-conducting layers with different lithology (and e.g. different magnetic susceptibility) could be distinguished from one another down to greater depths and interpreted with greater accuracy.

10. Conclusion

We demonstrated the successful applicability of novel semi-airborne EM systems by a validation of inversion results against established geophysical methods. Moreover, the use of various methods enabled the integrated interpretation of multiple geophysical, petrophysical and geological data.

We presented a 2.5D inversion result of the semi-airborne induction-coil data along a 7.5 km long reference profile, which was perpendicular to the regional geological strike direction. 2D ERT and LOTEM models along the same profile reached depths down to 1 km. Overall, the compared 2D resistivity models showed an excellent level of agreement, both, between each other and in comparison to geological information. We could clearly identify several good conductors with resistivities below 10 Ωm as Silurian alum shales. In detail, a few differences were observed between the three models, which could be explained by the varying locations of electric or magnetic data measurements, resolution capabilities of the methods, and IP- and 3D effects. In particular, ERT and LOTEM models were obtained using also the electric-field components, which increase the sensitivity towards deep structures and thus provide complementary information on the subsurface resistivity distribution, in contrast to HEM and semi-airborne EM cases, where only magnetic-field components were used. The determined conductive structures in the 2.5D inversions indicated depression zones of the complex graben structure of the Mühltroff transverse zone, in which Silurian alum shales were not removed.

The presented 3D semi-airborne EM model derived from SQUID data confirms that the assumption of the main strike direction justified the 2D inversions. The perspective 3D view of the various resistivity models shows very clearly that certain conductive structures can be followed

between the models of the different methods. A comparison of a clip of the 3D model at 50 m depth with the HEM models illustrates the good agreement as well. Additionally, the 3D view illustrates the different scales: The pure airborne EM (HEM) allows mapping on regional scale (here 445 km²) in a short time down to a relatively small depth (here about 150 m). With the ground-based methods ERT and LOTEM, investigation depths down to 1000 m or more can be achieved; due to the relatively complex setup, this is more feasible on a local scale (here a 7.5 km and 8.5 km long profile). The semi-airborne EM method combines the advantages of the strong ground-based transmitters to reach large penetration depths (here more than 500 m) with the advantages of the areal investigation (here 35 km²) of the airborne methods. We therefore classify the semi-airborne EM as intermediate scale.

The results of the semi-airborne EM surveys demonstrate independent realizations of the same method. The obtained 2D and 3D models were based on different instruments (induction-coil and SQUID magnetometer), used different processing codes (own code and KMSProMT) and different inversion codes (Mare2DEM and 3DINV). Despite these differences, both, the induction coil and the SQUID data sets yielded plausible models of the subsurface electrical resistivity, suggesting that the semi-airborne EM method itself is viable. Our results show that it is possible to detect conductive targets, such as mineral deposits, at great depths with both of the semi-airborne EM receiver systems.

Furthermore, we presented a multi-parameter approach for further interpretation. Borehole geophysical measurements from the historic mining area were statistically evaluated and rock samples petrophysically examined in the laboratory for supporting the geological interpretation of the geophysical models. We could conclude that diabase and alum shales should be most clearly distinguishable from each other in terms of geophysically measureable parameters. However, the value ranges of the physical parameters were extensive for most rock types and the explicit correlation with only a single parameter was hardly possible. Therefore, unique identification required a combination of multiple physical parameters, e.g., using clustering methods.

We applied an integrated interpretation method of regional scale geophysical data by a statistical approach. The developed method uses self-organizing maps (SOMs) to detect patterns in the distribution of resistivity, magnetic susceptibility, natural gamma radiation and gravity for comparison with geology. In a first approach, the cluster analysis was performed in a selected horizontal plane with data from HEM, HMG, HRD and gravimetry, and seven different lithological units were assigned. The derived SOMs compare well to geology. Since the

resistivity maps of HEM and semi-airborne EM are very similar in the near-surface region of our investigation area, it can be concluded that a similar SOM would be achieved with a semi-airborne EM map.

Declaration of Competing Interest

None.

Declaration of Competing Interest

The authors declare that they have no known competing financial interests or personal relationships that could have appeared to influence the work reported in this paper.

Appendix A. Appendicies

A.1. Appendix A. Lithostratigraphic table

Variscan unconformity			
Stratigraphy		**Lithology**	
Lower Carboniferous — Ziegenrück Fm.		graywacke	
Bordenschiefer Fm.		graywacke, clay shale	
Dachschiefer Fm.		clay shale	
Rußschiefer Fm.		C_{org} bearing clay shale	
Devonian — Schleiz Group		limestone, clay shale, quartzite, **diabase** in Berga Antiform	
Schwärzschiefer Fm.		black shale	
Tentakulitenschiefer Fm.		clay shale, (nereite-) quartzite	
Tentakulitenknollenkalk Fm.		limestone	
Silurian — Upper graptolit shale Fm.		clay shale, **alum shale**	
Ockerkalk Fm.		limestone	
Lower graptolite shale Fm.		**alum shale**, gravel shale	
Ordovician — Gräfenthal Group	Lederschiefer-Fm.	Diamictite (Gondwana Glaciation)	
	Schmiedefeld-Fm.	limestone, quartzite	
	Griffelschiefer-Fm.	C_{org} bearing clay shale, Fe-ore	
Phycodes Group		silt shale	
Weißelster Group		**phyllit**, quarzite	

Legend (right side):
- Lower Carboniferous
- Devonian and Silurian
- Ordovician Gräfenthal Group
- Ordovician Phycodes Group
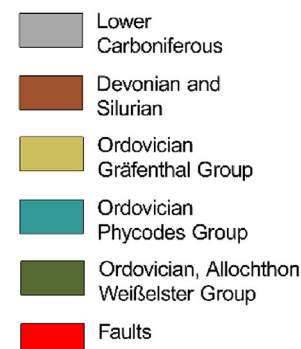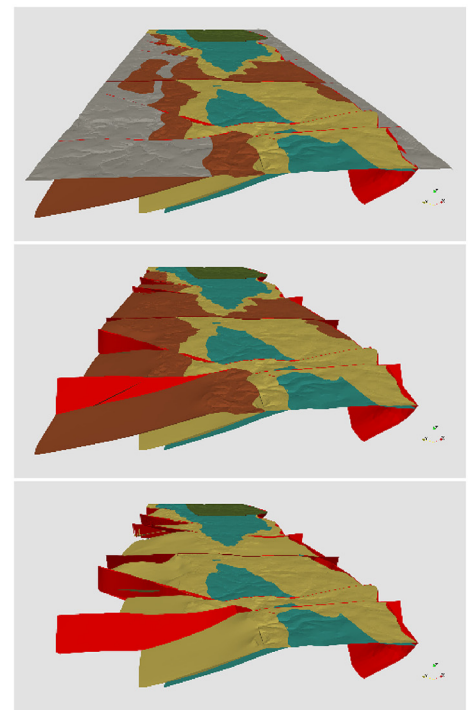- Ordovician, Allochthon Weißelster Group
- Faults

Fig. A.1. Left side: Lithostratigraphic table of the Berga anticline (after Sebastian, 2013). The colors of the stratigraphic boxes display the main colors of the geological overview map (Fig. 2), here the Silurian is indicated in blue. The colored frame lines above the lithology are associated with the colors of the layers in the 3D geological model (on the right side and Fig. 3). In this, Silurian and Devonian are joint together, which is indicated here by the missing blue frame line above the Silurian lithology. The lithological units that can best be distinguished by geophysical methods are printed in bold.

A.2. Appendix B. Examples of data and forward responses of each EM method at the reference profile

a. Helicopter-borne electromagnetic: HEM data, 1D inversion

b. Semi-airborne EM: induction coil data, 2.5D inversion

c. Semi-airborne EM: SQUID data, 3D inversion

d. Electrical resistivity tomography: ERT data, 2D inversion

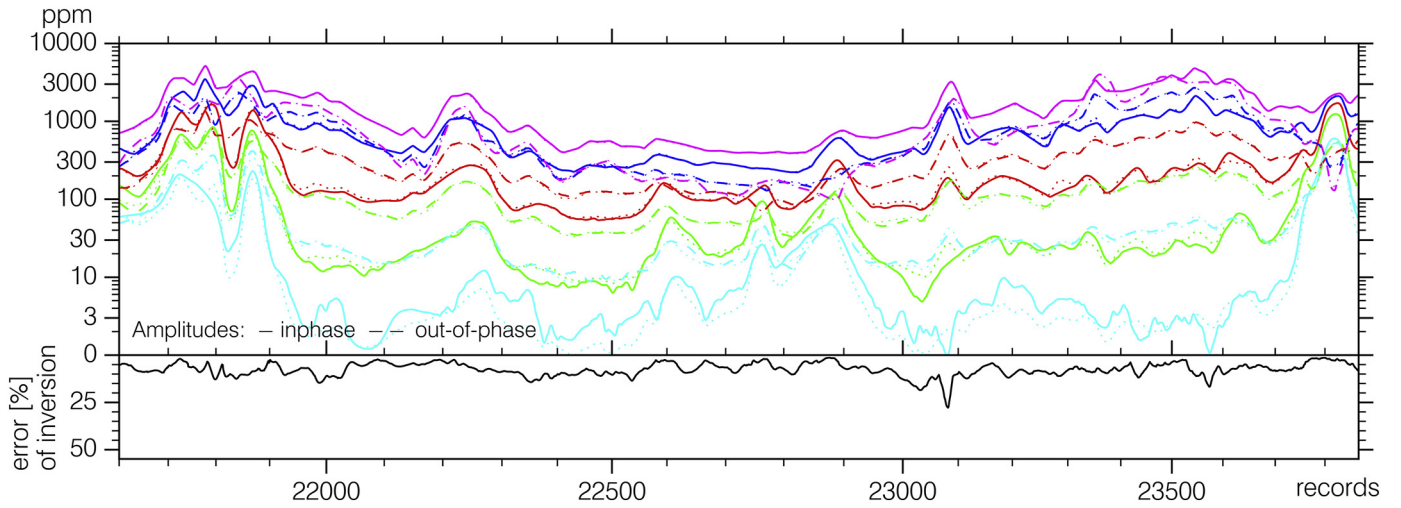e. Long-offset transient electromagnetics: LOTEM data, 2.5D inversion

Fig. A.2. Cross-section along a part of flight-line 17.1 of the HEM: Modeled (dotted) and processed inphase (solid) and quadrature (dashed) data of five frequencies (380 Hz (blue) – 130 kHz (pink)) with the misfit (fitting error of the inversion).
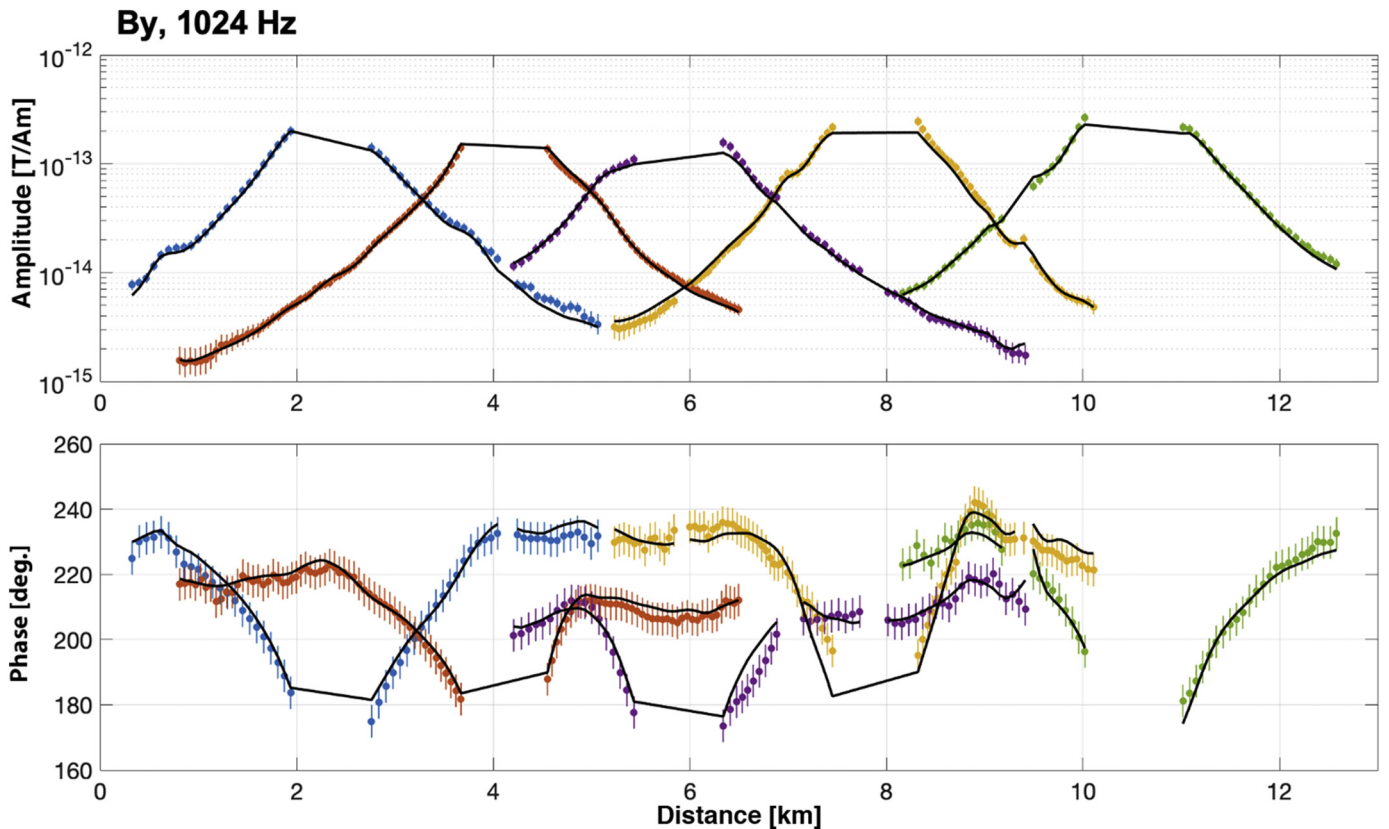

Fig. A.3. Example of semi-airborne induction-coil data in terms of amplitude and phase (colored symbols), the associated data errors and the model response (black lines) of the final inversion model along the reference profile. We display here the horizontal component in profile direction, labeled B_y, at a frequency of 1024 Hz.
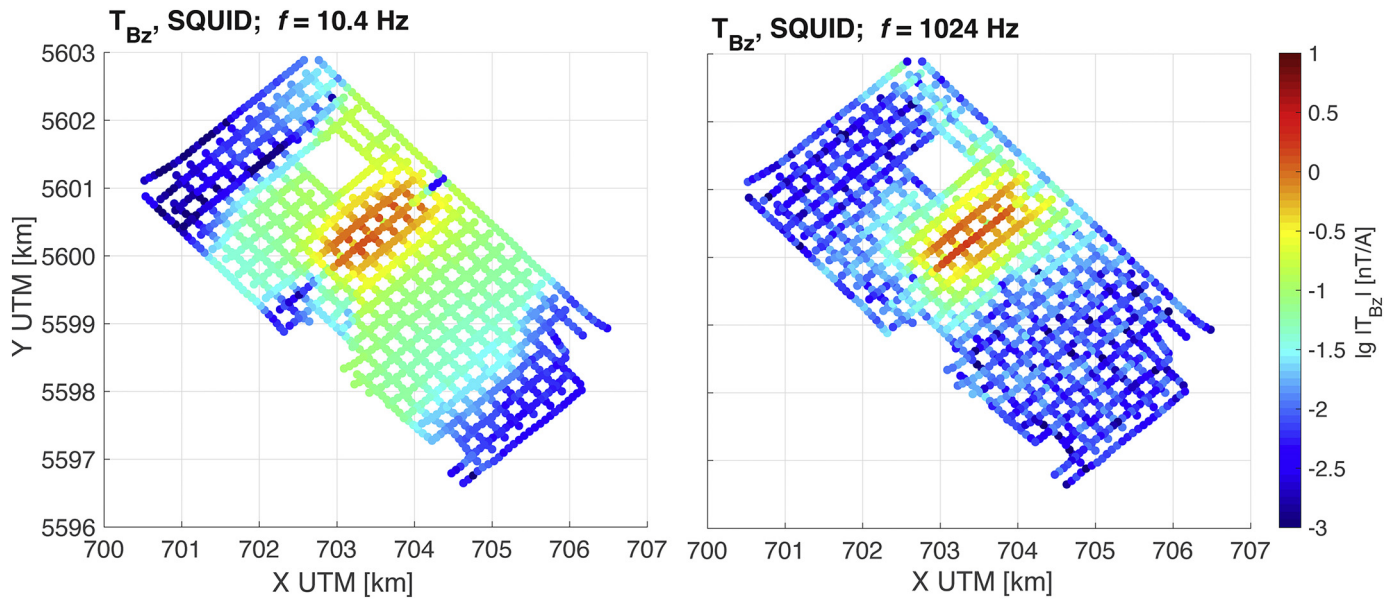
Fig. A.4. Map view of the transfer functions *TF* of the vertical component of the magnetic field (T_{Bz}) obtained from the semi-airborne SQUID data of subarea A7 at two frequencies: 10.4 Hz (left) and 1024 Hz (right). The consistent behavior of the data both at low and high frequencies is clear. The amplitude of the *TF* is the strongest (about 1 nT/A) in the vicinity (< 1 km) of the transmitter. At lower frequencies the field attenuates more gradually (0.1 nT/A at a distance of 4 km from the source) than at higher frequencies (0.01 nT/A at 2 km).
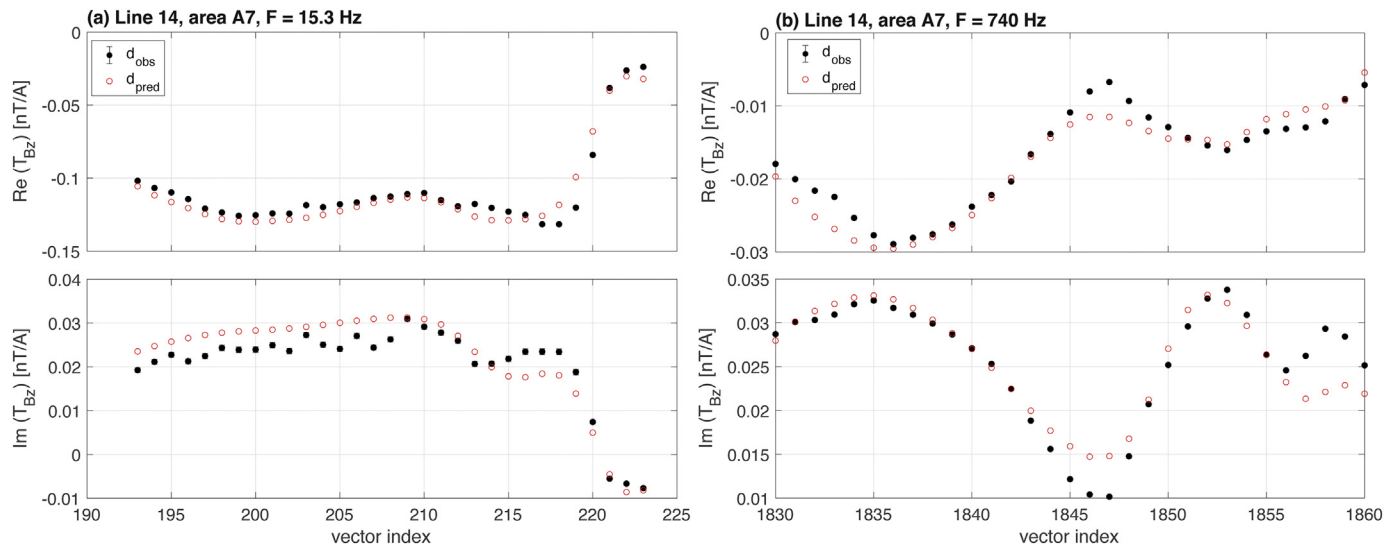

Fig. A.5. Example of the observed data (black circles) and model response (open red circles) along flight-line 14, subarea A7 for two frequencies 15.3 Hz and 740 Hz.
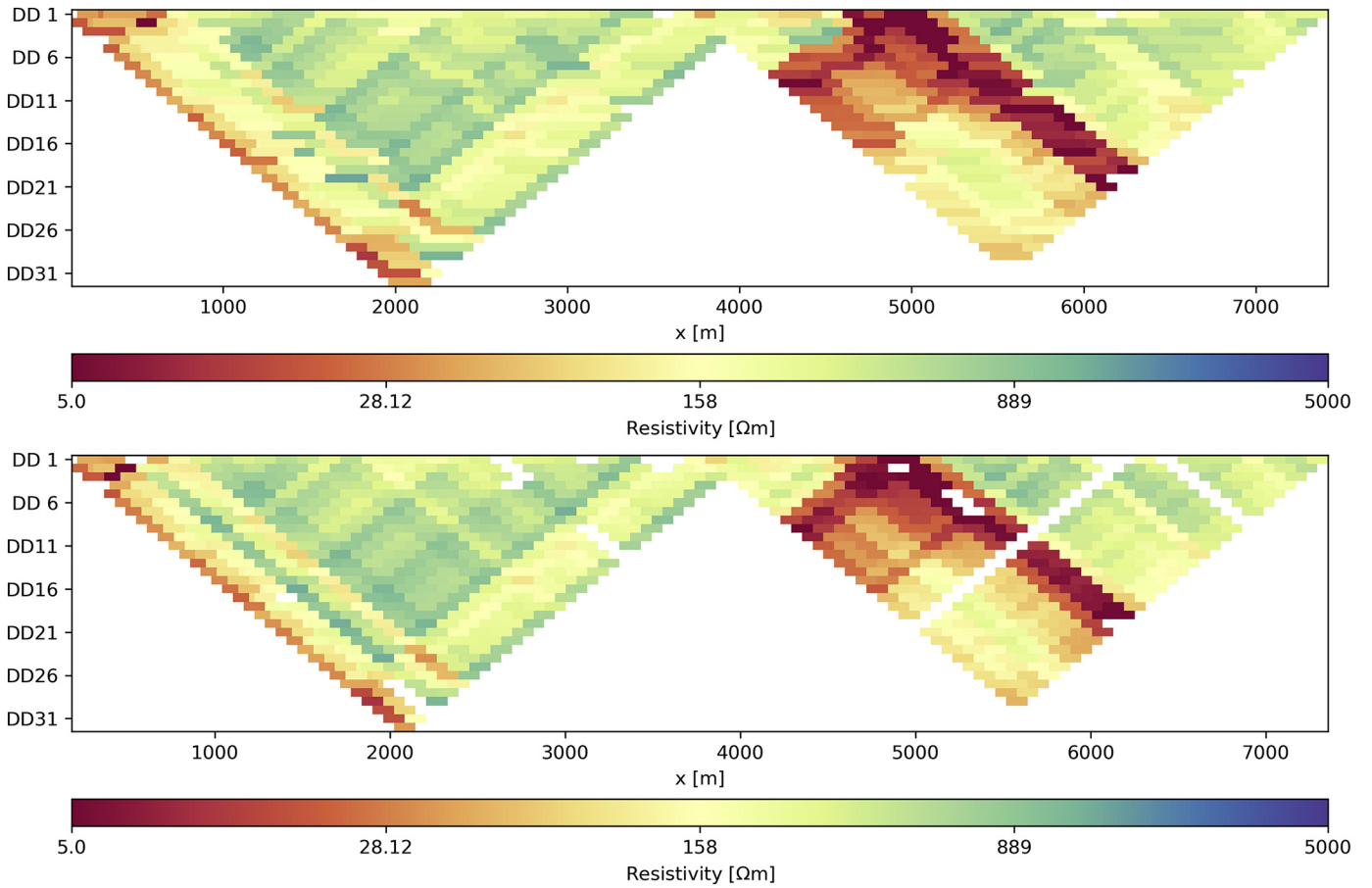
Fig. A.6. Observed pseudo-section of two overlapping ERT surveys (above) shown as apparent resistivities, the final model response (below). The vertical axis is the dipole-dipole n spacing, where DD26 indicates that the distance between the inner electrodes is 26 times greater than the dipole spacing (which is 105 m).
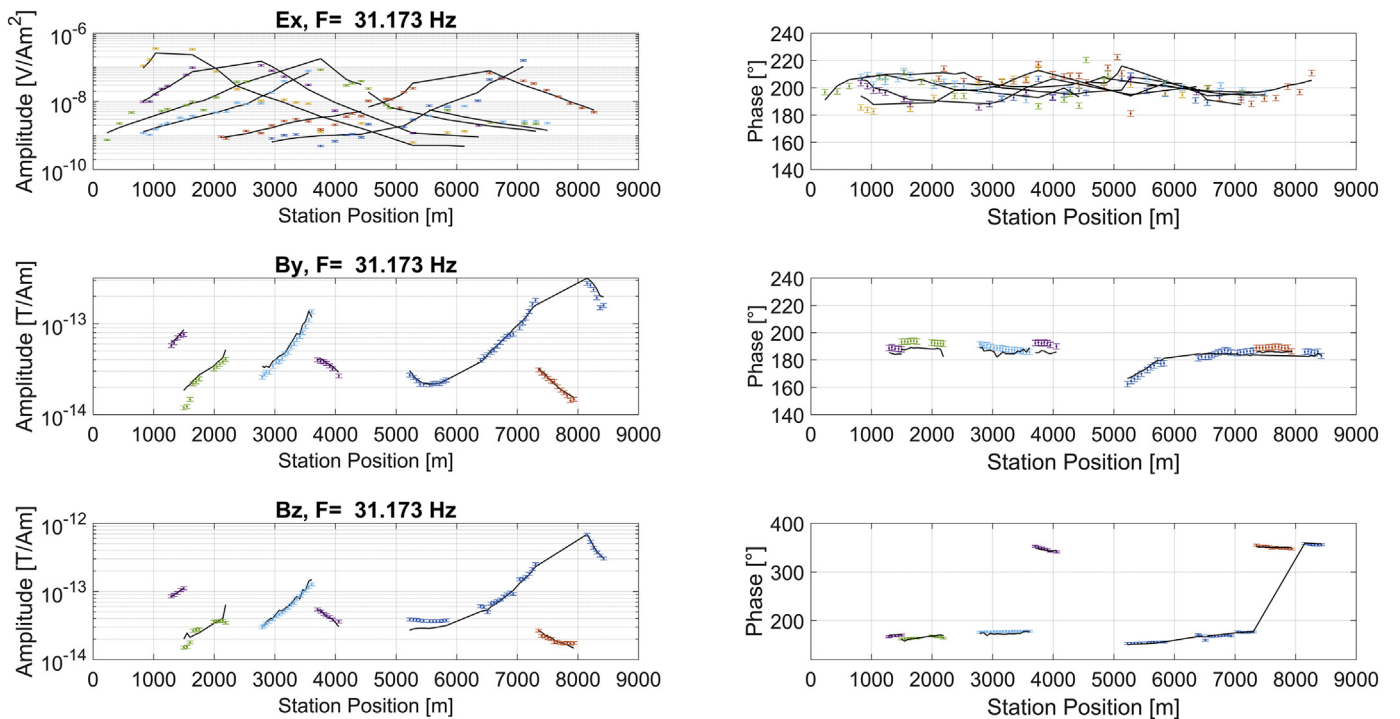

Fig. A.7. Observed (colored symbols) data, the associated data errors and the model response (black lines) of the final LOTEM inversion model exemplarily shown for one frequency (31 Hz). Displayed are the E_x, B_y and B_z component. Different colors correspond to different transmitters utilized.

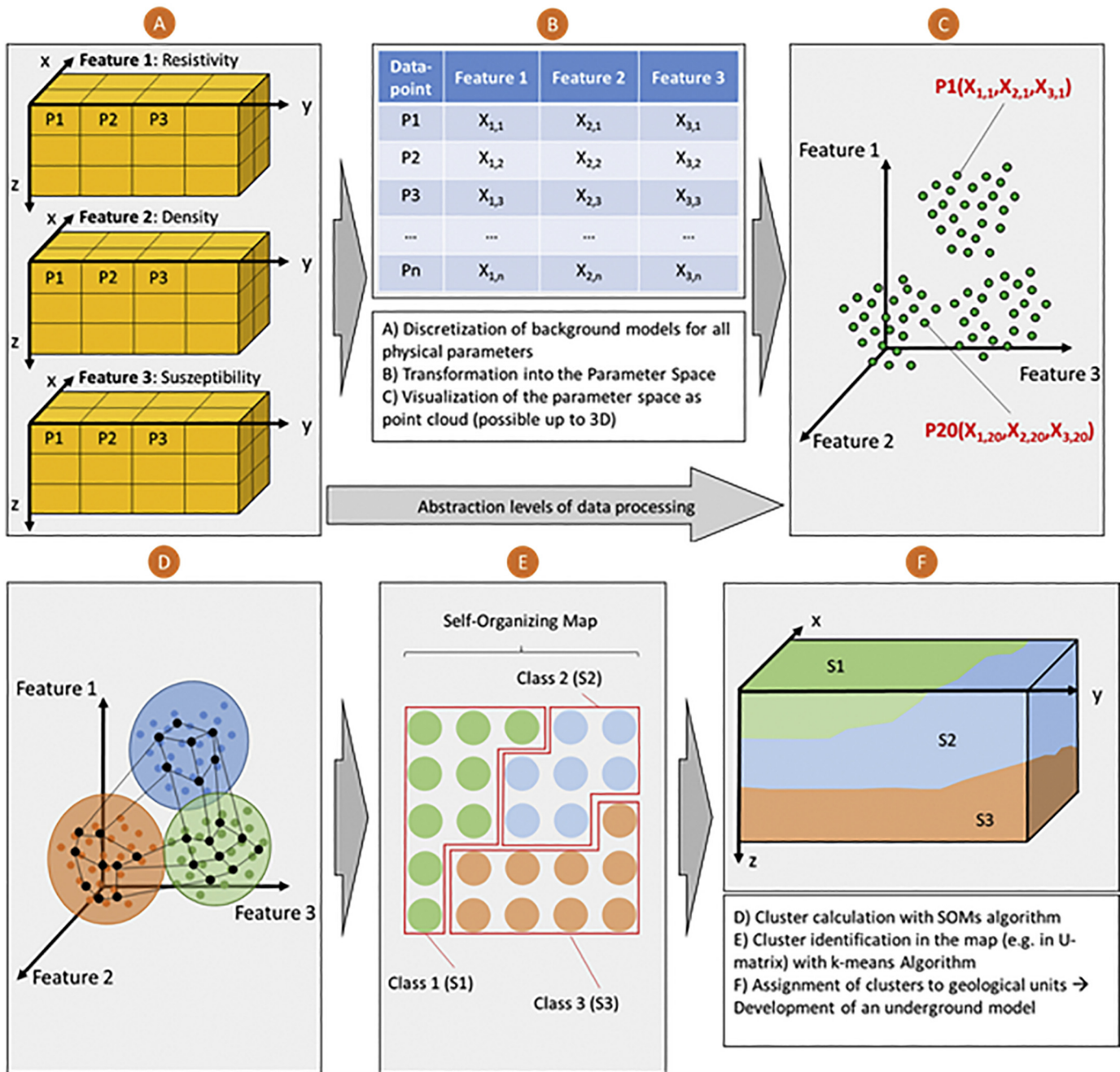**Appendix B. Appendix C. Principle of clustering using SOMs**

Fig. A.8. Principle of clustering using SOMs: A) First, the model space for all physical parameters is discretized. B) Then a transformation into the parameter space takes place, C) which can be visualized by point clouds. D) Using a SOMs algorithm, clusters of point clouds with similar parameters are formed and E) then transferred back into the model space (our map). F) At the end, the clusters are assigned to the geological units.

References

Abedi, M., Fournier, D., Devriese, S.G.R., Oldenburg, D.W., 2018. Integrated inversion of airborne geophysics over a structural geological unit: a case study for delineation of a porphyry copper zone in Iran. J. Appl. Geophys. 152, 188–202. https://doi.org/10.1016/j.jappgeo.2018.04.001.

Becken, M., Nittinger, C.G., Smirnova, M., Steuer, A., Martin, T., Petersen, H., Meyer, U., Mörbe, W., Yogeshwar, P., Tezkan, B., Matzander, U., Friedrich, B., Rochlitz, R., Günther, T., Schiffler, M., Stolz, R., DESMEX working group, 2020. DESMEX: a novel system development for semi-airborne electromagnetic exploration. Geophysics https://doi.org/10.1190/GEO2019-0336.1 In press.

BKG, 2012. Digital Topographic Model 1:200 000 (DTK200-V), Geobasisdaten: © GeoBasis-DE/BKG (2012), Bundesamt für Kartographie und Geodäsie. www.bkg.bund.de.

Chwala, A., Smit, J.P., Stolz, R., Zakosarenko, V., Schmelz, M., Fritzsch, L., Bauer, F., Starkloff, M., Meyer, H.-G., 2011. Low temperature SQUID magnetometer systems for geophysical exploration with transient electromagnetics. Supercond. Sci. Technol. https://doi.org/10.1088/0953-2048/24/12/125006.

Chwala, A., Kingman, J., Stolz, R., Schmelz, M., Zakosarenko, V., Linzen, S., Bauer, F., Starkloff, M., Meyer, M., Meyer, H.-G., 2013. Noise characterization of highly sensitive SQUID magnetometer systems in unshielded environments. Supercond. Sci. Technol. https://doi.org/10.1088/0953-2048/26/3/035017.

Costabel, S., Martin, T., 2019. Petrophysikalische Untersuchungen zum Befliegungsgebiet Schleiz/Greiz im Rahmen des BMBF-geförderten Projektes DESMEX, BGR Report, Archives No. 0135855, Hannover.

de Groot-Hedlin and Constable, 1990. OCCAM's inversion to generate smooth, two-dimensional models from magnetotelluric data. Geophysics 55 (12), 1613–1624. https://doi.org/10.1190/1.1442813.

Delsman, J.R., van Baaren, E.S., Siemon, B., Dabekaussen, W., Karaoulis, M., Pauw, P., Vermass, T., Bootsma, H., de Louw, P.G.B., Gunnink, J.L., Dubelaar, W., Menkovic, A., Steuer, A., Meyer, U., Revil, A., Oude Essink, G.H.P., 2018. Large-scale, probabilistic salinity mapping using airborne electromagnetics for groundwater management in Zeeland, the Netherlands. Environ. Res. Lett. 13 (8), 1–12. https://doi.org/10.1088/1748-9326/aad19e.

Dill, H., 1985. Antimoniferous mineralization from the Mid-European Saxothuringian Zone: mineralogy, geology, geochemistry and ensialic origin. Geol. Rundsch. 74 (3), 447–466.

Elliott, P., 1996. New airborne electromagnetic method provides fast deep-target data turnaround. Lead. Edge 15, 309–310.

Fountain, D., 1998. Airborne electromagnetic systems – 50 years of development. Explor. Geophys. 29, 1–11.

Gräbe, R., Schlegel, G., Wiefel, H., 1996. Digitale Geologische Karte von Thüringen, 1:25 000, Blatt 5436 Schleiz: Thüringer Landesanstalt für Umwelt und Geologie. Jena, Germany.

Grayver, A.V., Streich, R., Ritter, O., 2013. Threedimensional parallel distributed inversion of CSEM data using a direct forward solver. Geophys. J. Int. 193, 1432–1446. https://doi.org/10.1093/gji/ggt055.

Günther, T., Rücker, C., Spitzer, K., 2006. 3-D modeling and inversion of DC resistivity data incorporating topography – Part II: Inversion. Geophys. J. Int. 166, 506–517. https://doi.org/10.1111/j.1365-246X.2006.03011.x.

IAEA, 2003. Guidelines for Radioelement Mapping Using Gamma Ray Spectrometry Data. International Atomic Energy Agency. IAEA-TECDOC-1363AEA, Vienna.

Key, K., Ovall, J., 2011. A parallel goal-oriented adaptive finite element method for 2.5-D electromagnetic modelling. Geophys. J. Int. 186 (1), 137–154.

Kohonen, T., 2001. Self-Organizing Maps. 3rd ed. Springer https://doi.org/10.1007/978-3-642-56927-2 Switzerland 2014, ISBN 3-540-67921-9.

Krolop, P., Burisch, M., Richter, L., Fritzke, B., Seifert, T., 2019. Antimoniferous vein-type mineralization of the Berga Antiform, Eastern-Thuringia, Germany: a fluid inclusion study. Chem. Geol. 508, 47–61. https://doi.org/10.1016/j.chemgeo.2018.02.034.

LIAG, 2010. Schwerekarte der Bundesrepublik Deutschland 1:1 000 000, Bouguer – Anomalien. Leibniz-Institute for Applied Geophysics, Hannover.

Liebe, K, Zimmermann, T., E., Kaiser, E., Weise, E., 1912. Digitale Geologische Karte von Thüringen 1:25 000, Blatt 5437 Muehltroff: Thüringer Landesanstalt für Umwelt und Geologie, Jena, Germany.

Lines, L.R., Treitel, S., 1984. Tutorial: a review of least-squares inversion and its application to geophysical problems. Geophys. Prospect. 32, 159–186.

Liu, Y., Yogeshwar, P., Hu, X., Peng, R., Tezkan, B., Mörbe, W., Li, J., 2020. Effects of electrical anisotropy on long-offset transient electromagnetic data. Geophys. J. Int. https://doi.org/10.1093/gji/ggaa213.

Martin, T., Costabel, S., Günther, T., 2016. Methods for measuring the complex resistivity spectra of rock samples in the context of mineral exploration. Proceedings of 4th International Workshop of Induced Polarization, 6th – 8th June 2016, Aarhus Denmark.

Martin, T., Ibs-von Seht, M., Ullmann, A., Siemon, B., Pielawa, J., Steuer, A., Petersen, H., Voß, W., 2017. Technischer Bericht Hubschraubergeophysik Befliegung DESMEX, Teil 1, 175 Schleiz, Mai 2015, BGR Report, Archives No. 0134857, Hannover.

Meinhold, G., Hahn, T., Heuse, T., Mingram, B., 2005. Geochemistry and palynology of metasediments from the phyllite complex in the Greiz area (Saxo-Thuringia, Germany). N. Jb. Geol. Paläont. 237 (3), 423–452. https://doi.org/10.1127/njgpa/237/2005/423.

Meyer, U., Siemon, B., 2014. Hubschraubergeophysik der BGR neu am Start. Geowissenschaftliche Mitteilungen (GMIT) 55, 6–14.

Mogi, T., Tanaka, Y., Kusunoki, K., Morikawa, T., Jomori, N., 1998. Development of grounded electrical source airborne transient EM (GREATEM). Explor. Geophys. 29, 61–64.

Mörbe, W., 2020. Deep Controlled Source Electromagnetics for Mineral Exploration: A Multidimensional Validation Study in Time and Frequency Domain. Ph.D. thesis. University of Cologne.

Mörbe, W., Yogeshwar, P., Tezkan, B., Hanstein, T., 2020. Deep exploration using long-offset transient electromagnetics: Interpretation of field data in time and frequency domain. Geophys. Prospect. 68 (6), 1980–1998. https://doi.org/10.1111/1365-2478.12957.

Müller, F., Kroner, U., 2019. Tectonic 3D-Model of the Berga Antiform – Saxo-Thuringian Zone. GEOMÜNSTER 2019 Conference, Book of Abstracts. , p. 330. https://doi.org/10.13140/RG.2.2.16416.53767.

Nickschick, T., Flechsig, C., Mrlina, J., Oppermann, F., Löbig, F., Günther, T., 2019. Large-scale electrical resistivity tomography monitoring in the Cheb Basin (Eger Rift) at an International Continental Drilling Program (ICDP) monitoring site to image fluid-related structures. Solid Earth 10 (6), 1951–1969. https://doi.org/10.5194/se-10-1951-2019.

Nittinger, C.G., 2018. Development of a Semi-Airborne System and of Compressed Sensing Methods for Electromagnetic Imaging of the Subsurface. Ph.D. thesis. University of Münster.

Nittinger, C., Cherevatova, M., Becken, M., Martin, T., Petersen, H., Steuer, A., Meyer, U., Siemon, B., Matzander, U., Friedrichs, B., Mörbe, W., Yogeshwar, P., Tezkan, B., Rochlitz, R., Günther, T., 2017. A Novel Semi-airborne EM System for Mineral Exploration - First Results from Combined Fluxgate and Induction Coil Data. Second European Airborne Electromagnetics Conference, EAGE https://doi.org/10.3997/2214-4609.201702154.

Oppermann, F., Günther, T., 2018. A remote-control datalogger for large-scale resistivity surveys and robust processing of its signals using a software lock-in approach. Geosci. Inst. Methods Data Syst. 7, 55–66. https://doi.org/10.5194/gi-7-55-2018.

Pechnig, R., 2019. Interpretation von Bohrlochmessdaten aus Bohrungen Im Bereich des Bergaer Sattels – Thüringen. Geophysica Beratungsgesellschaft mbH, Explanatory report commissioned by the BGR, pp. 1–49. https://www.bgr.bund.de/DE/Themen/GG_Geophysik/Aerogeophysik/Projekte/abgeschlossen/DESMEX/Pechnig-2019-Interpretation-Bohrlochmessdaten.html?nn=1555598.

Petersen, H., Steuer, A., Siemon, B., Pielawa, J., Cherevatova, M., Günther, T., Yogeshwar, P., Schiffler, M., Arbeitsgruppe DESMEX, 2018. Befliegungsbericht DESMEX Projekt Semi-airborne Befliegung Hauptexperiment 183 Schleiz-Mühltroff, Oktober 2017. BGR Report, Archives No. 0135370, Hannover.

Petrow, J.W., Motz, H., Karwelis, G.A., Keßler, W., Müller, W., Pakulnis, G.W., Schuster, M., Kostin, N.E., Seidel, W., Gusjew, W.A., Nikonow, W.P., Wenke, R., Ungermann, M., 1972. Bericht über die Ergebnisse der Sucharbeiten im SW-Teil des Ostthüringischen Hauptsattels und der NW-Flanke des Hirschberg-Gefeller-Sattels (1966–1971), BAND 1, Sowjetisch-Deutsche Aktiengesellschaft "Wismut", Zentraler Geologischer Betrieb (Herausgeber). Geologisches Archiv der Wismut GmbH, Aue.

Preugschat, B., 2020. Erstellung eines integrierten 3D Untergrundmodells und Auswertung geophysikalischer Messungen mithilfe von künstlichen neuronalen Netzen anhand von geowissenschaftlichen Untersuchungen in Schleiz/Greiz in Thüringen, Deutschland. BGR Report, Hannover.

Reeves, C., 2005. Aeromagnetic Surveys: Principles, Practice & Interpretation. Geosoft https://pages.mtu.edu/~jdiehl/Homework4550/Aeromagnetic_Survey_Reeves.pdf.

Rochlitz, R., Queitsch, M., Yogeshwar, P., Günther, T., Chwala, A., Janser, S., Kukowski, N., Stolz, R., 2018. Capability of low-temperature SQUID for transient electromagnetics under anthropogenic noise conditions. Geophysics 83 (6), E371–E383. https://doi.org/10.1190/geo2017-0582.1.

Roy, B., Chakraborty, B.R., Bhattacharya, R., Dutta, A.K., 1978. Electrical and magnetic properties of antimony sulphide (Sb2S3) crystals and the mechanism of carrier transport in it. Solid State Commun. 25, 937–940.

Schiffler, M., Queitsch, M., Stolz, R., Chwala, A., Krech, W., Meyer, H.-G., Kukowski, N., 2014. Calibration of SQUID vector magnetometers in Full Tensor Gradiometry systems. Geophys. J. Int. 198, 954–964.

Schmelz, M., Stolz, R., Zakosarenko, V., Schoenau, T., Anders, S., Fritzsch, L., Mueck, M., Meyer, M., Meyer, H.-G., 2012. Sub-fT/Hz(1/2) resolution and field-stable SQUID magnetometer based on low parasitic capacitance sub-micrometer cross-type Josephson tunnel junctions. Physica C-Supercond. Appl. 482, 27–32.

Sebastian, U., 2013. Die Geologie des Erzgebirges. Springer Verlag, Berlin.

Sengpiel, K.P., Siemon, B., 2000. Advanced inversion methods for airborne electromagnetics. Geophysics 66, 1983–1992.

Siemon, B., 2006. Electromagnetic methods – Frequency domain: Airborne techniques. In: Kirsch, R. (Ed.), Groundwater Geophysics – A Tool for Hydrogeology. Springer, pp. 155–170.

Siemon, B., 2009. Levelling of frequency-domain helicopter-borne electromagnetic data. J. Appl. Geophys. 67 (3), 206–218. https://doi.org/10.1016/j.jappgeo.2007.11.001.

Siemon, B., Christiansen, A.V., Auken, E., 2009. A review of helicopter-borne electromagnetic methods for groundwater exploration. Near Surf. Geophys. 7, 629–646. https://doi.org/10.3997/1873-0604.2009043.

Siemon, B., Steuer, A., Ullmann, A., Vasterling, M., Voß, W., 2011. Application of frequency-domain helicopter-borne electromagnetics for groundwater exploration in urban areas. J. Phys. Chem. Earth 36 (16), 1373–1385.

Siemon, B., Costabel, S., Voß, W., Meyer, U., Deus, N., Elbracht, J., Günther, T., Wiederhold, H., 2015. Airborne and ground geophysical mapping of coastal clays in Eastern Friesland, Germany. Geophysics 80 (3), WB21–WB34. https://doi.org/10.1190/geo2014-0102.1.

Siemon, B., van Baaren, E., Dabekaussen, W., Delsman, J., Dubelaar, W., Karaoulis, M., Steuer, A., 2019. Automatic identification of fresh–saline groundwater interfaces from airborne electromagnetic data in Zeeland, the Netherlands. Near Surface Geophys. 17, 3–25. https://doi.org/10.1002/nsg.12028.

Skiba, P., 2011. Homogene Schwerekarte der Bundesrepublik Deutschland (Bouguer-Anomalien). Projekt: Anomalienkarten von Potenzialfeldern, LIAG, Hannover, access 1/31/2019.

Smirnov, M.Y., 2003. Magnetotelluric data processing with a robust statistical procedure having a high breakdown point. Geophys. J. Int. 152, 1–7. https://doi.org/10.1046/j.1365-246X.2003.01733.x.

Smirnov, M., Becken, M., Nittinger, C., Yogeshwar, P., Mörbe, W., Rochlitz, R., Steuer, A., Costabel, S., Smirnov, M., DESMEX Working Group, 2019. A novel semi-airborne frequency-domain CSEM system. Three-dimensional inversion of semi-airborne data from the flight experiment over an ancient mining area near Schleiz, Germany. Geophysics 84 (5), E281–E292. https://doi.org/10.1190/GEO2018-0659.1.

Smirnova, M., Juhojuntti, N., Becken, M., Smirnov, M., Yogeshwar, P., Steuer, A., Rochlitz, R., Schiffler, M., DESMEX Working Group, 2019. Combined 3D Inversion of Ground and Airborne Electromagnetic Data over Iron Ore in Kiruna. Ext. Abstr. Conference Proceedings, 25th European Meeting of Environmental and Engineering Geophysics, 5p https://doi.org/10.3997/2214-4609.201902446.

Smith, R., 2014. Electromagnetic induction methods in mining geophysics from 2008 to 2012. Surv. Geophys. 35 (1), 123–156.

Smith, R.S., Annan, A.P., McGowan, P.D., 2001. A comparison of data from airborne, semi-airborne, and ground electromagnetic systems. Geophysics 66, 1379–1385.

Steuer, A., Siemon, B., Eberle, D., 2008. Airborne and Ground-based Electromagnetic Investigations of the Freshwater potential in the Tsunami-hit Area Sigli, Northern Sumatra. J. Environ. Eng. Geophys. 13 (1), 39–48.

Steuer, A., Siemon, B., Auken, E., 2009. A comparison of helicopter-borne electromagnetics in frequency and time-domain at the Cuxhaven valley in Northern Germany. J. Appl. Geophys. 67, 194–205. https://doi.org/10.1016/j.jappgeo.2007.7.001.

Steuer, A., Martin, T., Siemon, B., Meyer, U., 2016. Projekt DESMEX: Lagerstättensuche in Thüringen – Vorerkundung Mit HEM. Abstracts Book of the 76st Annual Meeting of the German Geophysical Association (DGG), Münster, 2-H.003. https://doi.org/10.2312/dgg76.

Strack, K.M., 1992. Exploration with Deep Transient Electromagnetics. Elsevier, Amsterdam.

Tølbøll, R.J., Christensen, N.B., 2007. Sensitivity functions of frequency-domain magnetic dipole-dipole systems. Geophysics 72, F45–F56.

Toloczyki, M., Trurnit, P., Voges, A., Wittekindt, H., Zitzmann, A., 2006. Geologische Karte der Bundesrepublik Deutschland 1:1 000 000 (GK1000). Bundesanstalt für Geowissenschaften und Rohstoffe Hannover.

Vallée, M.A., Smith, R.S., Keating, P., 2011. Metalliferous mining geophysics— State of the art after a decade in the new millennium. Geophysics 76 (4), W31–W50. https://doi.org/10.1190/1.3587224.

Wu, X., Xue, G., Fang, G., Li, X., Ji, Y., 2019. The development and application of the semi-airborne electromagnetic system in China. IEEE Access 7. https://doi.org/10.1109/ACCESS.2019.2930961.

Yang, D., Oldenburg, D.W., 2016. 3D inversion of total magnetic intensity data for time-domain EM at the Lalor massive sulphide deposit. Explor. Geophys. 48 (2), 110–123.

Zampa, L., 2019. Gravity Data Processing and Modelling for the Investigation Area of Schleiz-Greiz. BGR Report, Archives No. 0136394, Hannover.

Zhdanov, M.S., 2010. Electromagnetic geophysics: notes from the past and the road ahead. Geophysics 75 (5), 75A49–75A66. https://doi.org/10.1190/1.3483901.